Electronic Theses and Dissertations, 2004-2019

2015

Phase Transformations and Microstructural Evolution in the U-10 wt.% Mo Alloy with Various Zr Additions at 900C and 650C

Nicholas Eriksson
University of Central Florida

Showcase of Text, Archives, Research & Scholarship

PHASE TRANSFORMATIONS AND MICROSTRUCTURAL EVOLUTION IN THE U-10WT% MO ALLOY WITH VARIOUS ZR ADDITIONS AT 900˚C AND 650˚C

by

NICHOLAS ERIKSSON
B.S. University of Florida 2012

A thesis submitted in partial fulfillment of the requirements
for the degree of Master of Science
in the Department of Material Science and Engineering
in the College of Engineering and Computer Science
at the University of Central Florida
Orlando, Florida

Fall Term
2015

Major Professor: Yongho Sohn

ABSTRACT

The Reduced Enrichment for Research and Test Reactor (RERTR) now known as the Material Minimization and Management Reactor Control program (MMMRC) seeks to replace the use of highly enriched uranium (HEU) fuels used in research and test nuclear reactors around the world. The low enriched uranium (LEU) fuels must have fissionable uranium densities comparable to the HEU fuels. After extensive investigation by various researchers around the world, the U-Mo alloys were selected as a promising candidate. The Mo alloyed with U allows for the stabilization of the face-centered cubic γ-U phase, which demonstrated favorable irradiation behavior. However, deleterious diffusional interaction between the fuel and the cladding, typically Al-base alloy, remain a challenge to overcome for application of U-Mo alloys as the LEU fuel.

Zr has been identified as a potential diffusion barrier between monolithic U-10 wt.% Mo (U10Mo) metallic fuel and AA6061 cladding alloys for the development of a LEU fuel system. However, interdiffusion and reaction between the Zr barrier and U10Mo fuel can produce phases such as Mo_2Zr, and promote the destabilization of γ-U phase into γ'-U (U_2Mo) and α-U. In order to better understand this phenomenon, this study examined the phases that are present in the U10Mo alloys with varying Zr concentration, 0, 0.5, 1.0, 2.0, 5.0, 10.0, 20.0 wt.% at room temperature after heat treatment at 900°C for 168 hours and 650°C for 3 hours. These two temperatures are relevant to fuel plate fabrication process of homogenization and hot-rolling, respectively. Scanning electron microscopy and X-ray

diffraction were employed to identify and quantitatively document the constituent phases and microstructure to elucidate the nature of phase transformations.

For U10Mo alloys containing less than 1.0 wt.% Zr, there was no significant formation of Mo_2Zr after 900˚C homogenization and subsequent heat treatment at 650˚C for 3 hours. The γ-U phase also remained stable correspondingly for these alloys containing less than 1.0 wt.% Zr. For U10Mo alloys containing 2 wt.% or more Zr, a significant amount of Mo_2Zr formation was observed after 900˚C homogenization and subsequent heat treatment at 650˚C for 3 hours. For these alloys, destabilization of γ-U into γ'-U (U_2Mo), UZr_2 and α-U was observed. The alloy containing 20 wt.% Zr, however, did not demonstrate γ-U decomposition even though Mo_2Zr was observed after heat treatments. The formation of Mo_2Zr effectively reduced the stability of the metastable γ-U phase by depleting the γ-stabilizing Mo. The destabilization of γ-U phase into the α-U phase is not favorable due to anisotropic and poor irradiation behavior of α-U phase. Therefore the formation of Mo_2Zr at the interface between U10Mo fuel and Zr diffusion barrier must be carefully controlled during the fabrication of monolithic LEU fuel system for successful implementation.

ACKNOWLEDGMENTS

With the sincerest gratitude I thank everyone involved in this project. The journey to a master's degree was fraught with trials and tribulations, however with the support of my co-researchers, family, and friends I have managed to get through this.

First and foremost Dr. Yongho Sohn with his everlasting patience and faith has pushed me to places I didn't think I could go. Dr. Sohn has been compassionate, understanding, and a role model. He has truthfully been an everlasting impact on my life and I will never forget the lessons, both easy and very hard, he has taught me throughout my graduate career.

Dr. Kevin Coffey and Dr. Challapalli Suryanarayana have shown me great insight into the worlds of material science. Dr. Coffey with his innate compassion has supported me through hard times and has allowed me this important opportunity. Dr. Suryanarayana with his wisdom of material science and his wonderful teaching ability has bolstered my interest in material science and goaded me to pursue this path. I'm eternally grateful to what you have provided me.

Last but not least, the MCF staff and to my lab-mates, for their patience with me in my efforts, their ability to listen and give advice when need be, and their ability to cheer me up when in need, I thank you. My experience at the University of Central Florida would not have been the same without every single one of you.

TABLE OF CONTENTS

LIST OF FIGURES

LIST OF TABLES

CHAPTER 1: INTRODUCTION

Growing public concern for the potential weaponization of exported highly enriched uranium (HEU) fuels prompted the inception of the Reduced Enrichment for Research and Test Reactors (RERTR) program in 1978, now known as the Material Management and Minimization Reactor Conversion (MMMRC) program. The primary goal of the RERTR program was the development of necessary technologies to eliminate the need for HEU fuel usage in modern reactors. This goal could be achieved by increasing the U density present in low enriched uranium (LEU) fuels to approach the performance of HEU fuel [1].

A promising candidate determined by the RERTR program to be used in the replacement of HEU fuels with LEU fuels was U-Mo [2-4]. The U-Mo system allows for the stabilization of the γ-U phase by lowering the temperature at which the γ-U $\rightarrow$ α–U transformation occurs from 668°C to 560°C [5]. This reduces the amount of deleterious anisotropic swelling observed under irradiation and during fabrication [5]

Initial fuel forms used in testing potential LEU fuels involved atomized and machined particles of U-Mo embedded into an Al matrix and covered in an AA6061 cladding layer. These fuels can contain a U density of up to 8.5g/cm^3 [6]. A significant amount of interdiffusion between the fuel and matrix caused swelling under irradiation [2-4]. With enough swelling during operation, the fuel would experience mechanical failure. To reduce the potential of this and meet higher U density requirements [7], a monolithic plate fuel form using a U-10wt% Mo (U-10Mo) alloy was investigated and tested [1]. Monolithic plates allowed for a much higher U density to be achieved and lowered the amount of interfacial area prone to interaction between

the U-Mo and the Al cladding. Even with a reduced interaction surface area, porosity was observed at the interface in the monolithic fuels after irradiation. This porosity was caused by fission gas bubbles which resulted in delamination [1]. This prompted the need for a diffusion barrier between the meat and cladding, Zr was a promising candidate [7].

Research has been done on Mo and Nb as diffusive barriers as well [8]. Even though reaction rates for Mo and Nb were 100x and 1000x slower than Zr, the Nb exhibited thermal cracking due to expansion mismatch and the Mo was not suitable for thermomechanical processing [8].

Zr was chosen as a diffusion barrier due to the slow interactions observed between the Zr/Al interface in the monolithic fuel plate as well as the favorable irradiation stability of the reaction products [7,8]. Zr also exhibits favorable thermal conductivity and melting temperature [9], low neutron absorption rate and cross section [10], and corrosion resistance [11], all important considerations when choosing a diffusive barrier for this system.

To form the monolithic fuel plate, a hot isostatic process (HIP) has been developed and utilized by Idaho National Labs (INL) [12]. Previous investigations into the interactions between fuel meat (U10Mo), diffusion barrier (Zr), and cladding layer (AA6061) during the HIP process have been carried out utilizing interdiffusion to better understand the interaction zones in the U-10Mo/Zr/AA6061 system [13-15]. Huang *et* al. reported interdiffusion of U-10Mo and Zr at temperatures above 600˚C [13]. Perez *et* al. observed numerous phases in the U-10Mo/Zr interface after the entire hip process was completed which includes a HIP step at 560˚C [15]. Park *et* al. studied the effect of time and temperature on the U-10Mo/Zr interface around HIP

temperatures (520˚C-560˚C) [14]. Prior to the HIP process, there is a homogenization step and a hot rolling step

The objective of this study was to examine the microstructural development and constituent phases in U-10Mo+xZr alloys with varying Zr content, x=0, 0.5, 1, 2, 5, 10, 20 wt.%, quenched from 900˚C and 650˚C corresponding to the homogenization and hot-rolling process prior to HIP for monolithic fuel manufacturing. X-ray diffraction (XRD) and scanning electron microscopy (SEM) with X-ray energy dispersive spectroscopy (XEDS) were employed to identify and quantify phase constituents. Findings from this study helped to understand how the interdiffusion between the U10Mo fuel and Zr diffusion barrier affected the intermetallic formation and phase stability of γ-U solid solution with respect to fuel processing. The starting microstructure and phase constituents would have a significant influence on the performance of the fuel during irradiation.

CHAPTER 2: LITERATURE REVIEW

History of RERTR and Initial Fuel Research

In 1953 President Dwight D. Eisenhower addressed the United Nations with "Atoms for Peace", an article outlining the importance of shifting nuclear attention from war to energy production [16]. Great strides were made, by 1970 the US was exporting 700kg of HEU annually. RERTR was established to reduce the potential weaponization of these HEU fuels by replacing them with LEU fuels.

Initially, three dispersion type fuels were tested, uranium silicides, uranium aluminide, and uranium oxide [17]. Favorable U_3Si_2 results led to the implementation of a U_3Si_2-Al fuel to replace a majority of the HEU fuels used in reactors, which were UAl_x-Al and U_3O_8-Al [18]. Higher power reactors still needed a more dense U fuel to replace the current HEU fuels in use, so the RERTR program began investigations into the two types of fuel materials that were capable of attaining high enough densities, U_6Tx (Tx being a transition metal) and U alloys containing a very small amount of alloying elements. Unsatisfactory fuel performance was observed from two transition metal compounds, U_6Fe-Al and U_6Mn-Al These compounds were tested by Hofman [19] and Meyers [20], respectively, and poor irradiation behavior was observed and assumed for the rest of the transition metal compounds. RERTR-1 and RERTR-2 tested U dispersion samples with low percentages of alloying elements. Table 1, shows the 11 alloys tested listed by γ-U phase stability. From this screening test it was concluded that U alloys with at least 6 wt.% Mo (U-6Mo) exhibited low swelling and stable irradiation behavior [3] with

U-10Mo exhibiting the lowest swelling [2]. Because of the very promising U-Mo behavior,

further studies were done on the phase evolution and decomposition of the U-Mo system.

Table 1 U alloys tested for RERTR-1 and RERTR-2 (alloying elements presented in wt.%) [1]

High γ Stability	Medium γ Stability	Low γ Stability	Precipitate Dispersion within Fuel Particles
U-10Mo U-8Mo U-9Nb-3Zr	U-6Mo U-6Mo-1Pt U-6Mo-0.5Ru U-6Nb-4Zr	U-5Nb-3Zr U-4Mo U-2Mo-1Nb-1Zr	U-10Mo-0.05Sn U-6Mo-0.1Si

<u>Fuel Forms under RERTR</u>

Dispersive Fuel Plates

U densities of fuels used in reactors at the inception of RERTR were up to 3.2g-U/cm^3

for HEU fuel. A higher U-density was achievable utilizing dispersion type fuels, U_3Si_2-Al fuels

with a U density of 4.8g/cm^3 [1]. Dispersion type fuels were made of U alloys encased in an Al

matrix with an AA6061 cladding around the entire sample as shown in Figure 1.
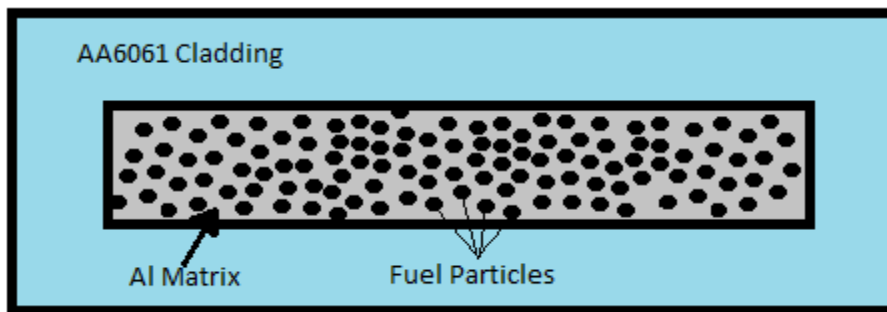
Figure 1 Schematic of a dispersion fuel mini-plate

Dispersion particles were obtained by gas atomization and occasionally fuel filings [2]. These powders were formed into mini-plates by using standard powder metallurgy methods to combine the uranium and aluminum powders. The compact was then incased in an AA6061 frame and cover plates. The assembled sample was then welded shut, hot rolled, then cold rolled to the appropriate size for the given experiment [17]. These dispersion fuels have a large amount of fuel surface area which tends to favor interdiffusion and reaction. This same large surface area also allows for potential oxidation to occur during fabrication which can ultimately lead to blistering upon plate formation. Dog-boning can also occur while hot rolling, which is a relative thinning of the center of the specimen compared to the edges caused by a difference in hardness between the fuel meat and the cladding. Yet another potential issue that dispersion fuels encountered was small raised areas which were caused by larger/thicker than expected particles being used in the compacts. This in effect causes localized dog-boning and clad thinning in that area [17]. It was also observed that the dispersion fuel plates exhibited fission bubble formation after irradiation as shown in Figure 2 [2].
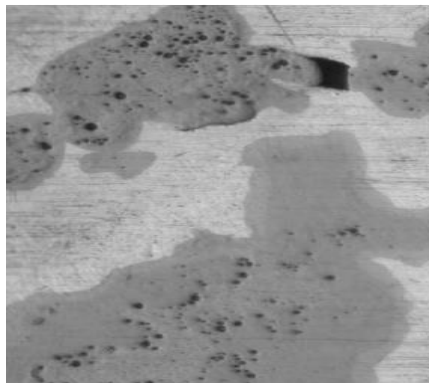
Figure 2 U-6Mo dispersion fuel exhibiting fission bubbles after irradiation [2]

Monolithic Fuel Plates

As mentioned before, higher powered reactors needed a higher U density fuel. To achieve this, monolithic fuel plates schematically drawn in Figure 3, were developed, and a hot isostatic pressing (HIP) process was used to manufacture.

Prior to the HIP process, Idaho National Laboratory (INL) developed a 7 step process to prepare the U10Mo alloys. The process starts with arc-melting of the alloy, forming it into an ingot using a graphite coupon mold. The ingot is then laminated to the Zr diffusion barrier using a canned assembly and hot rolling which causes interdiffusion and interactions between the layers of the fuel coupon and prompts investigation of the system. The canned assembly involves placing the U alloy between two Zr foils and then perimeter welding the edges prior to rolling. In initial studies, the fuel foil was laminated directly to the AA6061 cladding. However, Al cladding/fuel interactions prompted the use of a diffusion barrier [1,2,7]. To laminate the Zr onto the U10Mo ingot, a hot rolling process at 650˚C is utilized. This hot rolling involves a preheating step at 650-700˚C for up to one hour followed by 2-4 passes of hot rolling and reheating at 650˚C for several minutes. This reheating and rolling process is repeated from 10-20 times each time increasing the force incrementally. The rolling schedule contains a reduction of pass force at the 165 minute mark which follows a 30 minute reheat. This causes a less aggressive thinning in subsequent passes and prevents mechanical abnormalities such as ripples to develop in the fuel coupon during rolling. The hot rolling process is then followed by a 650˚C anneal for 30-120 minutes. Prior to the HIP process, the U10Mo/Zr coupons are sanded and cleaned with a nitric/hydrofluoric acid rinse. The AA6061 cladding material is also cleaned and roughened to

promote favorable bonding surfaces. The U10Mo/Zr and AA6061 are then loaded into a HIP can which is then edged welded shut in an Ar glovebox. The sealed HIP can is then vacuum degassed at 315°C for 3-4 hours utilizing a roughing pump and lamination of the AA6061 to the Zr is carried out at 560°C and 100MPa for 60 minutes [12]. Increased fissionable U density as well as the reduction of fission bubble formation due to a reduced interacting surface area between fuel meat and cladding causes a more favorable and predictable irradiation behavior.

Figure 3 Schematic diagram of U10Mo-Zr-AA6061 monolithic fuel plate

Phase Equilibria of Binary Systems

U-Mo

Previous studies have shown that UMo alloys, specifically those containing at least 6 wt.% Mo show favorable irradiation behavior/performance [2-5]. The cubic nature of γ-U and its equal coefficients of thermal expansion, resulting in isotropic behavior, make it a desirable phase in nuclear applications due to its isotropic swelling behavior. As seen in the U-Mo phase diagram in Figure 4, the U10Mo γ solid solution undergoes a eutectoid reaction at 555°C.
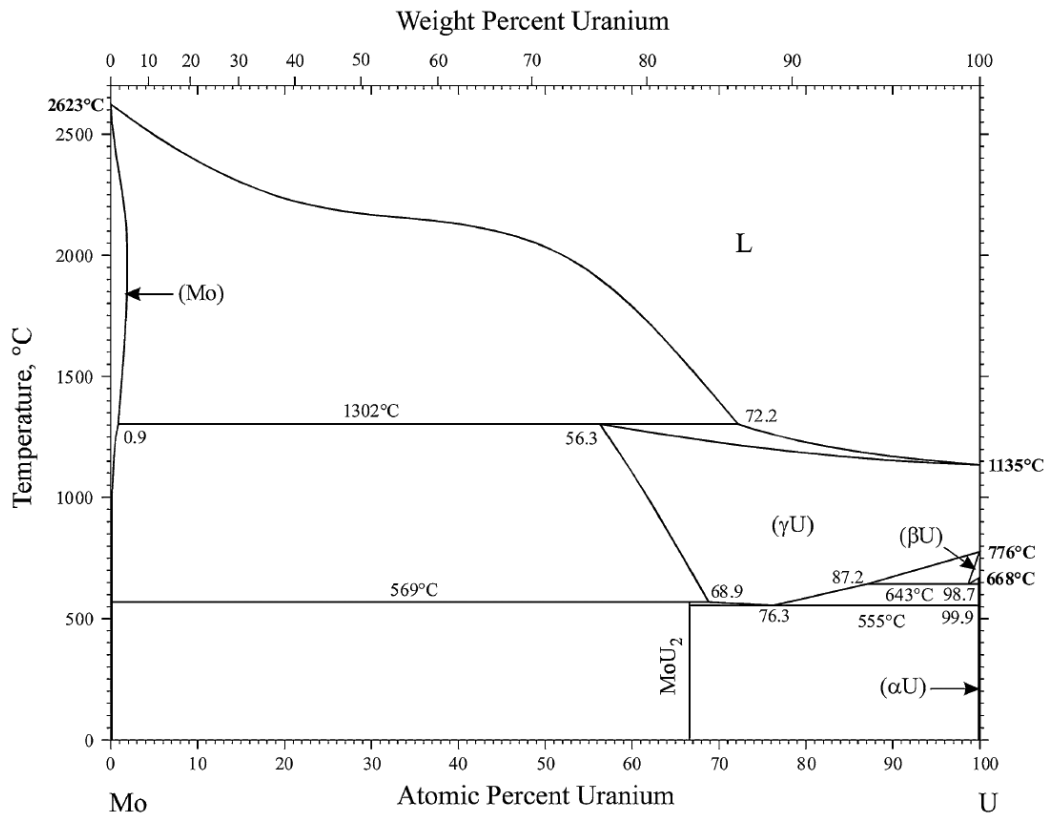
Figure 4 Equilibrium U-Mo binary phase diagram [5]

The eutectoid decomposition yields orthorhombic α-U and body centered tetragonal γ'
(U$_2$Mo). An example of this is presented in Figure 5 which shows a eutectoid reaction gone to
completion after 14 days at 500˚C.
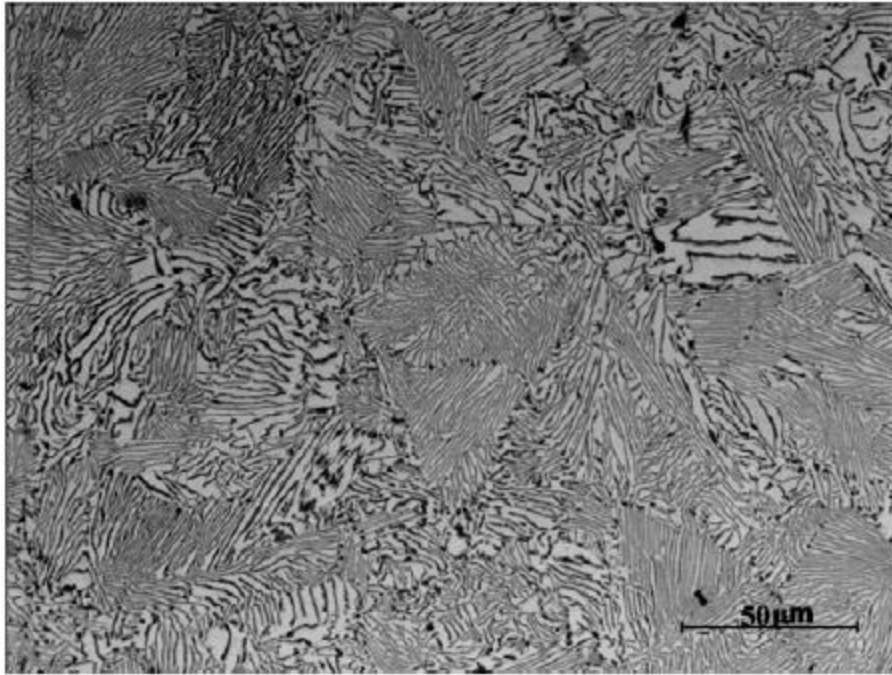
Figure 5 Backscattered micrograph of U-9 wt.% Mo after a 14 day anneal at 500˚C [5]

The anisotropic swelling caused by α-U's coefficients of thermal expansion can lead to catastrophic failure of the fuel due to internal stress and strain imparted onto the system during irradiation. By adding Mo to the U, the γ transformation temperature changes from 776˚C (at 0 wt.% Mo) to 560˚C (at 10 wt.% Mo) effectively stabilizing the phase at lower temperatures. β-U forms between 668˚C and 776˚C, and has not been observed frequently. At 17 wt.% Mo, γ can transform into γ' at 580˚C as determined by differential thermal analysis, dilatometry, and differential scanning calorimetry by Kutty *et* al. [21].

U-Zr

Binary U-Zr studies have shown that the formation of the δ-Zr or UZr_2 phase along with α-U phases can occur upon γ (U,Zr) decomposition as shown in Figure 6.
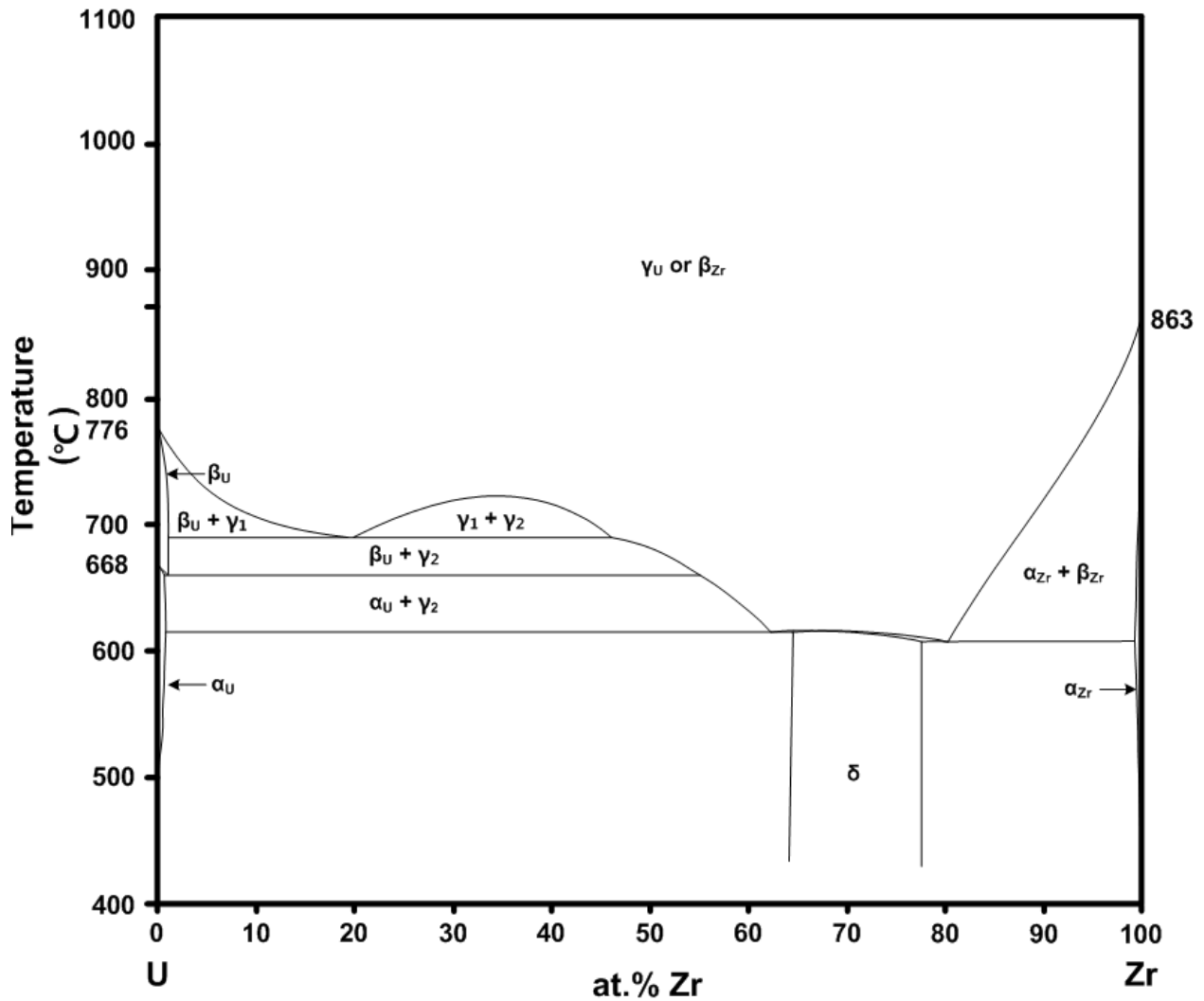
Figure 6 Equilibrium U-Zr binary phase diagram [22]

According to the phase diagram in Figure 6, at 1000°C there is a (γU,βZr) solid solution which is stable up to around 1135°C without Zr. This phase undergoes a reaction at 776°C forming β-U. This reaction occurs at 693°C at around 5 wt.% Zr. Subsequent cooling will impose a second reaction which forms α-U at 662°C. Cooling below 617°C forms an α-U and δ-UZr$_2$. The γ-U to α-U transition involves both a martensitic and non-martensitic α transformation .

Figure 7 depicts a 900˚C anneal on a U-2 wt.% Zr sample which was carried out for 120 hours and water quenched.
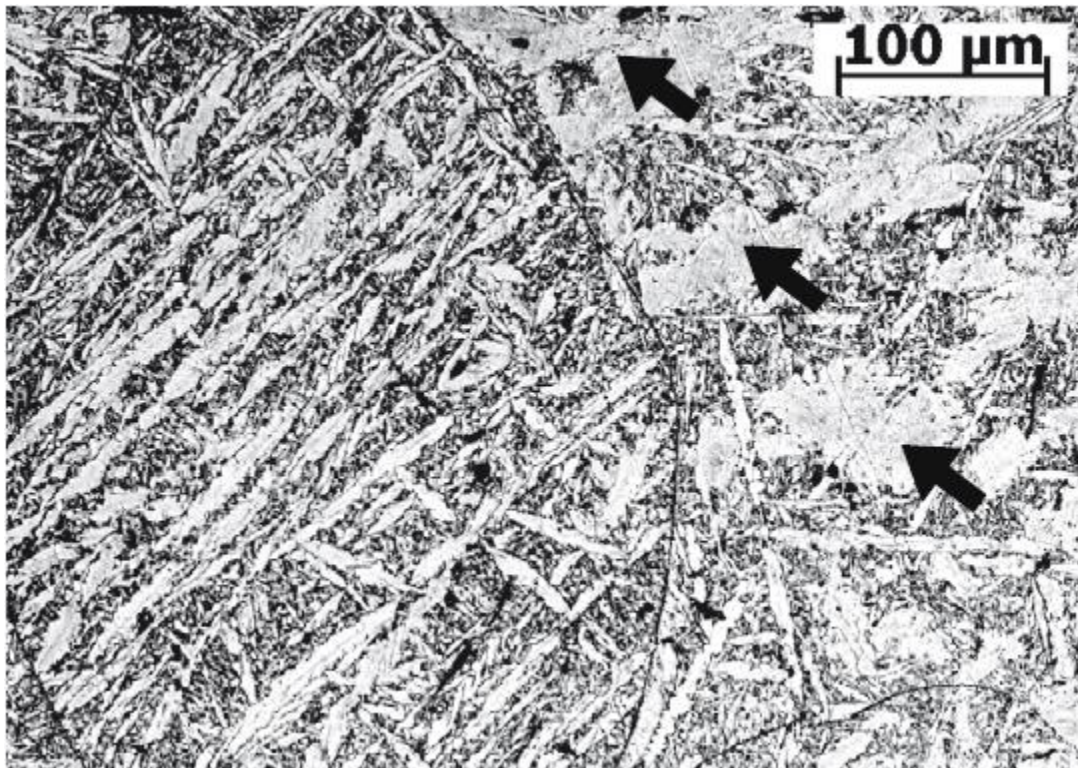
Figure 7 U-2 wt.% Zr annealed for 120 hours at 900˚C and water quenched, arrows indicate non-martensitic α-U [22]

The micrograph in Figure 7 depicts both the non-martensitic α (arrows) and the needle like martensitic/acicular α phases with prior γ-U grains visible. With the rapid cooling of water quenching, one would assume the transformation takes place in one step, however C. Basak *et al.* used dilatometry to show that the γ-U phase actually undergoes 2 transformations, γ-U → α''(monoclinic) → α_m (orthorhombic). Basak also showed that slower cooling rates favor less martensitic α formation [22].

Mo-Zr

Given the previous studies on U-Zr and U-Mo alloys, this study focused on the alloying

of all 3 components and the subsequent decomposition that occurs at temperatures under 1000˚C.

An understanding of the Mo-Zr interactions below this temperature is needed to understand the

potential phases which can form in this ternary system. Previous diffusion studies by A. Paz y

Puente show that under 1050˚C the interface between Mo and Zr has one intermetallic phase

Mo_2Zr and a β-Zr solid solution as shown in Figure 8 [23]. Supporting this information, Perez

did a thermodynamic assessment on the Mo-Zr binary phase diagram which is displayed in

Figure 9 [24]. With these studies it is logical to observe that under 1000˚C, a Mo_2Zr phase will

form.
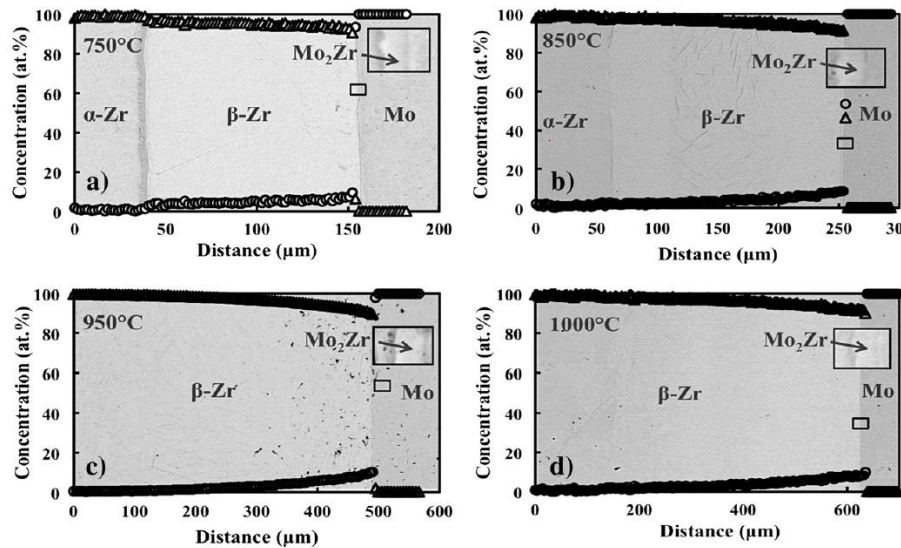
Figure 8 Mo-Zr diffusion couple study results as determined by XEDS at a) 750˚C, b)850˚C, c)950˚C and d) 1000˚C demonstrating Mo_2Zr formation [23]
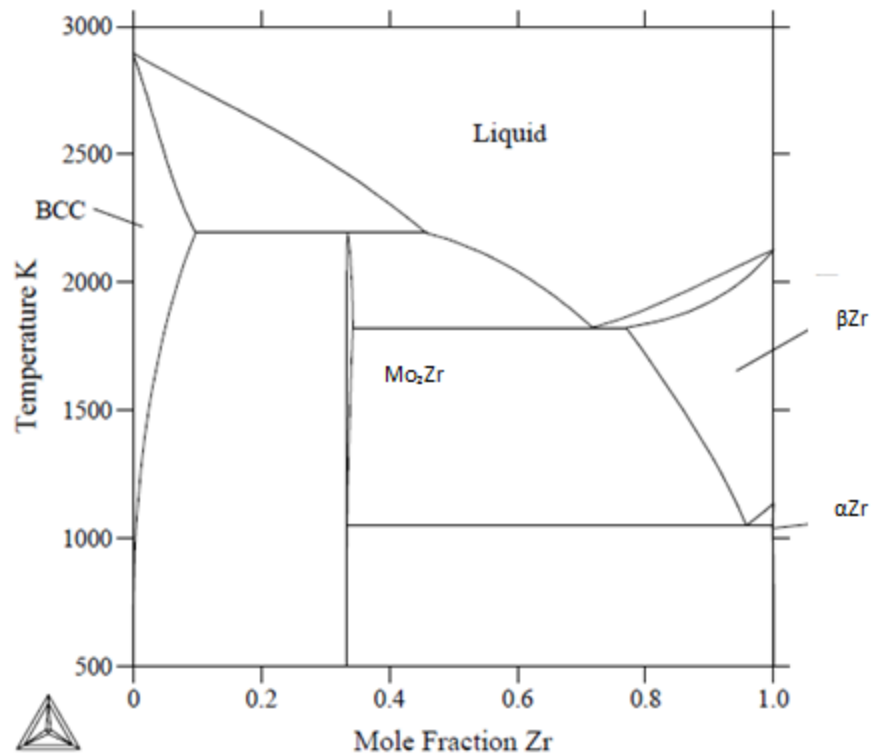
Figure 9 Equilibrium Mo-Zr binary phase diagram [24]

UMo vs Zr

Huang used diffusion studies at temperatures from 600˚C-1000˚C to investigate the U10Mo/Zr interface and found that only Mo_2Zr forms along the interface and a β-Zr solid solution on the Zr rich side of the interface [13]. Perez et al. studied the diffusion of U10Mo and Zr after the HIP process. Perez found that at the U10Mo/Zr interface, UZr_2, α-U, and Mo_2Zr have formed [15]. Park *et* al. confirmed these results and further noted that, at 520˚C-560˚C with various hold times, no significant additional UZr_2, Mo_2Zr, or α-U growth was observed. Park also concluded, that at the 650˚C hot-rolling step, is where these phases seem to develop [14].

14

Phase Equilibria and Time Temperature Transformation in the Ternary U-Mo-Zr System

Ternary U-Mo-Zr

Ivanov *et* al. did an experimental study on the potential phases in the U-Mo-Zr system at

1000˚C-625˚C [25]. Structural data for the U-Mo-Zr ternary phases are presented in Table 2 [25].

Figure 10 depicts the equilibrium ternary phase diagram the U-Mo-Zr system at 1000˚C. Lack of

a 900˚C ternary phase diagram prompted the use of the 1000˚C diagram from Ivanov.

According to Ivanov's phase diagram, at 1000˚C [25], Figure 10, three phases are

possible, γ-U, Mo_2Zr, and Mo. The BCC Mo is only present at very high Mo concentrations. The

Mo_2Zr intermetallic compound is present at its stoichiometric composition on the phase diagram.

The γ-U solid solution has a very broad solubility range and demonstrates higher solubility with

Zr than with Mo. Between the Mo_2Zr and γ-U phase regions there exists a large two phase region

in which Mo_2Zr can form. At relatively high Mo concentrations there is a three phase region

between Mo, γ-U, and Mo_2Zr.

In Figure 11, an equilibrium ternary phase diagram for the U-Mo-Zr system at 650˚C is

presented from Ivanov [25]. The diagram depicts the potential of six phases in this system at this

temperature. The phases possible are β-U, α-U, γ-U, Mo_2Zr, α-Zr, and Mo. β-U is only present at

high U concentrations with very low Zr and Mo content. α-U is similar in that it requires high U

content and low Zr and Mo concentration, however it forms two and three phase regions with γ-

U and Mo_2Zr at various concentration ranges. β-U, however, forms a very small two phase

region with γ-U at extremely low Zr concentrations. γ-U demonstrates three solubility ranges in

the 650˚C equilibrium. A low Zr concentration γ-U between 15 and 35 at.% Mo, an intermediate

one containing about 30 at.% Zr and 10 at.% Mo., and a Zr rich γ-U phase containing 85 at.% Zr

and 5 at.% Mo. All three γ-U solid solutions form a two phase region with α-U. The two lower

Zr content γ-U phases form a 3 phase region with α-U and Mo_2Zr. The high and intermediate Zr

content γ-U can form a three phase region including Mo_2Zr.

Table 2 Structural data for potential phases from the equilibrium ternary phase diagrams of the
U-Mo-Zr system at 1000˚C and 650˚C [25]

Phase	Formula	Pearson Symbol	Space Group
(U,Zr)ht	U, γ-U	cI2	Im-3m
(U) ht1	U, β-U	tP30	$P4_2$/mnm
(U) ht2	U, γ-U	cI2	Im-3m
(U)rt	U, α-U	oC4	Cmcm
(Mo)	Mo; γ-Mo	cI2	Im-3m
(Zr) rt	Zr, α-Zr	hP2	$P6_3$/mmc
$ZrMo_2$	Mo_2Zr	cF24	Fd3m
U_2Mo rt	U_2Mo	tI6`	I4/mmm
UZr_2 rt	UZr_2	hP3	P6/mmm

1000˚C
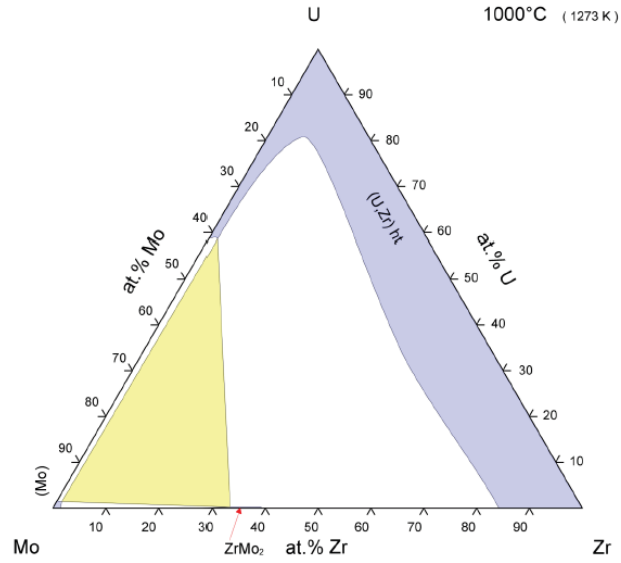
Figure 10 Ternary equilibrium phase diagram of U-Mo-Zr at 1000˚C [25]

650˚C
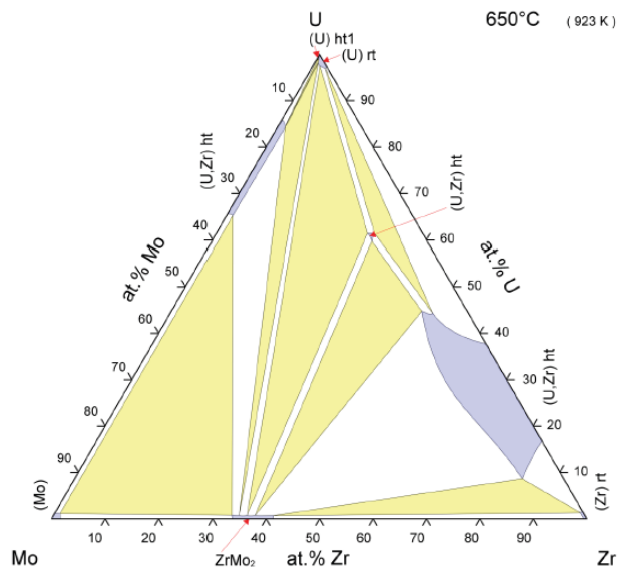
Figure 11 Ternary equilibrium phase diagram of U-Mo-Zr at 650˚C [25]

17

Time Temperature Transformation Curves

U-Mo

In Figure 12 and Figure 13 Repas *et* al. presented a U8Mo and U10Mo TTT diagram, respectively, after quenching to temperature from 900˚C [26].
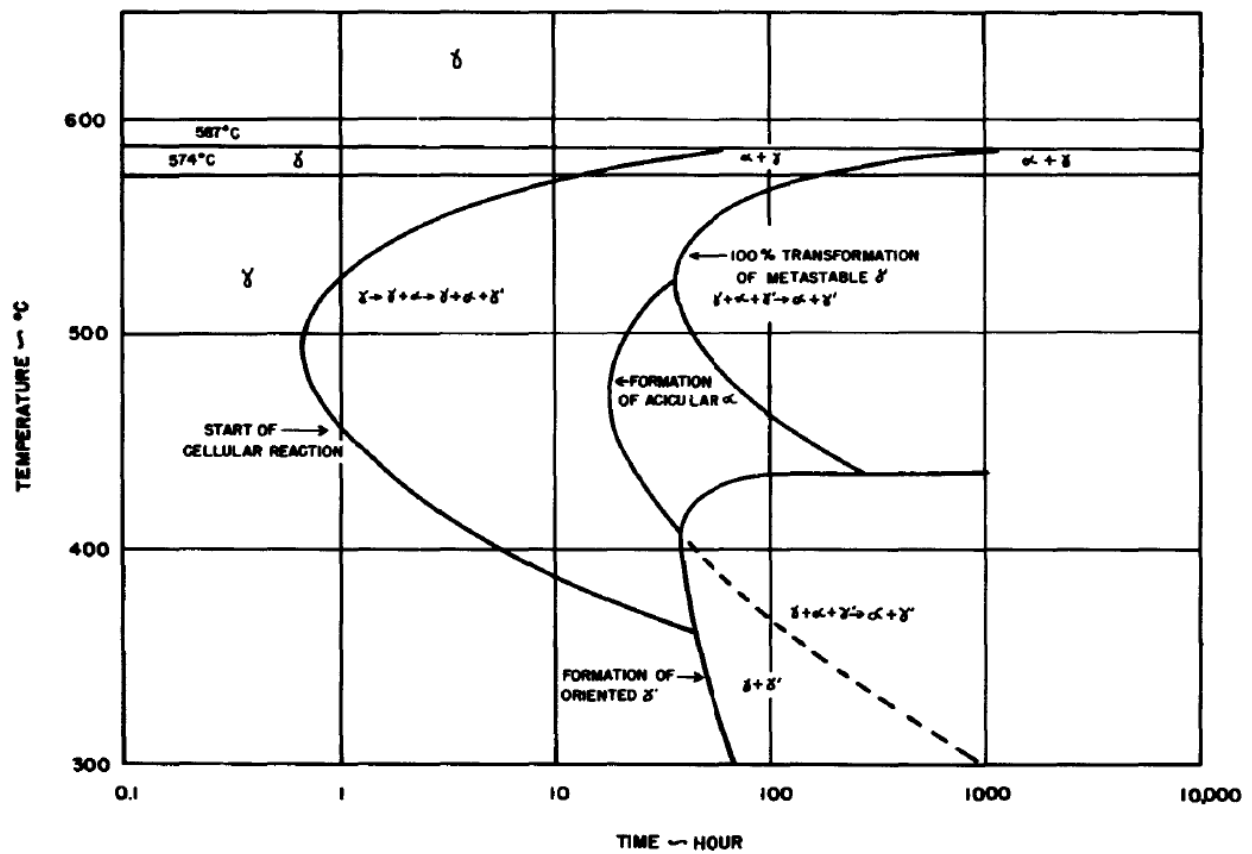
Figure 12 Time temperature transformation patterns for U8Mo quenched to temperature after a 900˚C anneal [26]
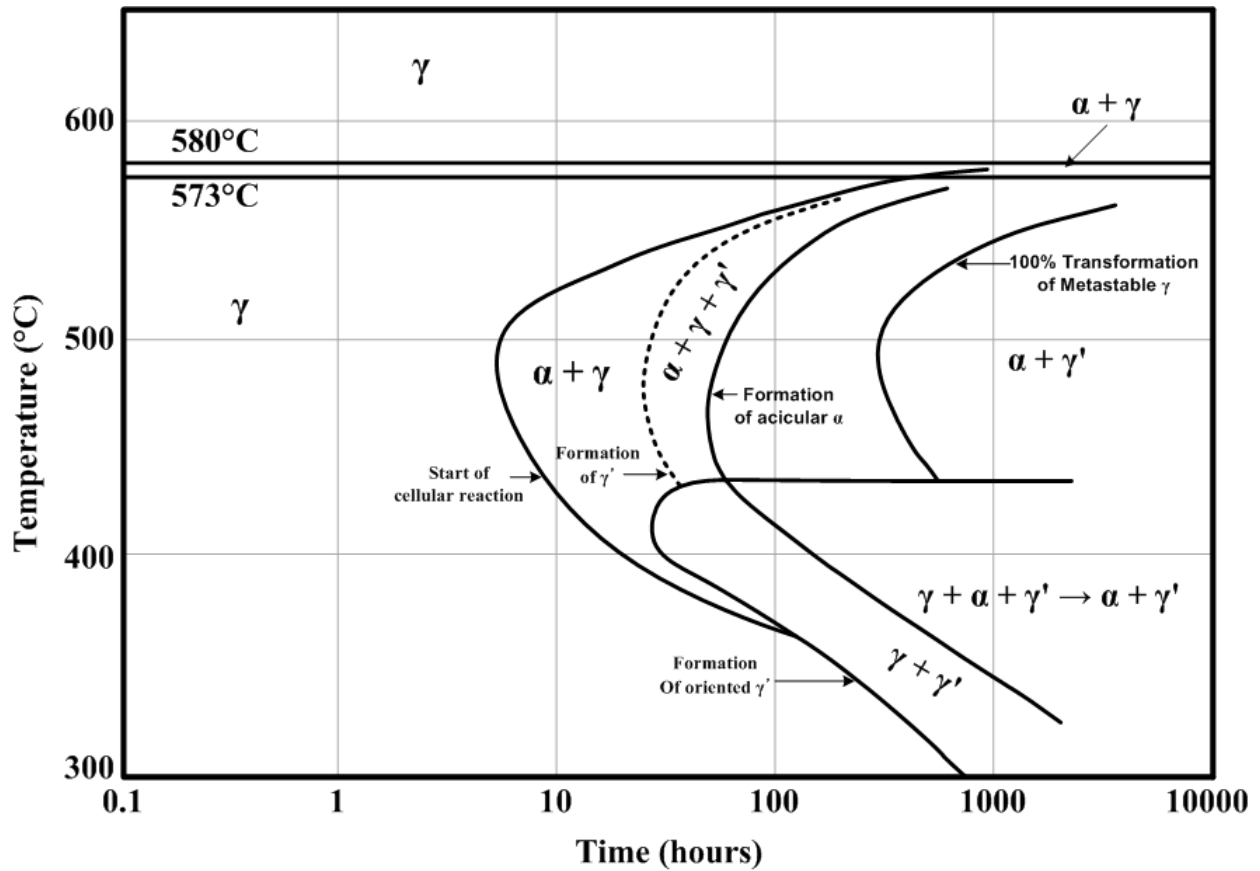
Figure 13 Time temperature transformation curves for U10Mo quenched to temperature after a 900˚C anneal [26]

First thing to note is that with a decrease in Mo concentration, a decrease in nucleation time of α-U occurs. The transformation occurs as such, $\gamma \rightarrow \gamma + \alpha \rightarrow \gamma + \alpha + \gamma'$ with acicular α forming before a complete transformation, and oriented γ' forming at slow cooling rates. The reaction forming acicular α occurs more rapidly in lower Mo content U-Mo alloys as well. With lower Mo concentration it is predicted that a faster nucleation of acicular α and a slower nucleation of oriented γ' could occur.

U-Mo-Zr

Figure 14 shows the TTT diagram of U-10Mo with various Zr compositions, 0.0, 1.0, 2.0, 4.0, and 6.0 wt.% Zr, presented by Peterson *et* al. [27].
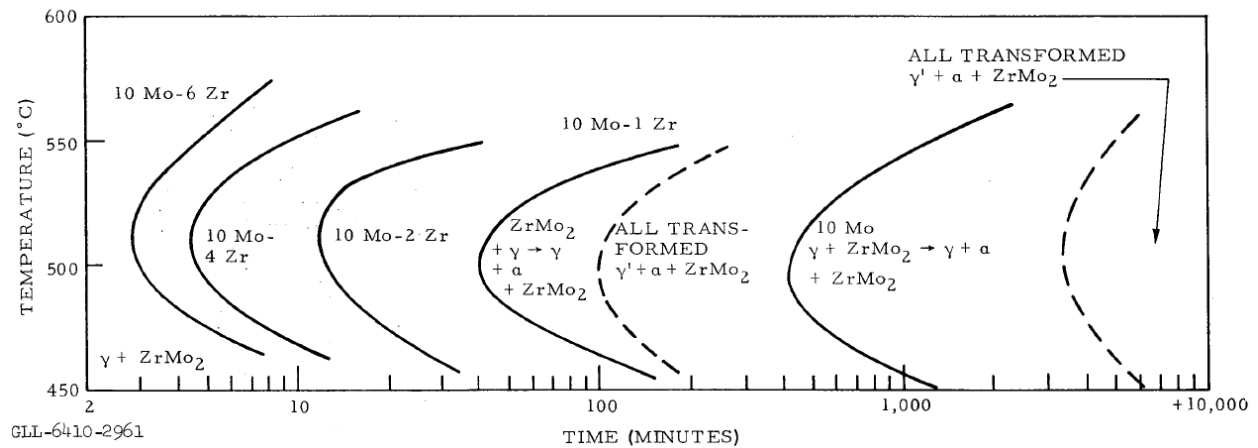
Figure 14 Effect of Zr on UMo alloys displayed in a TTT diagram[27]

Higher Zr composition pushes the nose of the TTT diagram to shorter times. With only a 6 wt.% Zr content, the reaction nucleates after around 3 minutes at 560˚C, the HIPing temperature. With 10 and 20 wt.% Zr, and assuming the observed trend continues, one can then assume almost instantaneous reaction. As seen from the difference in time to 100% transformation between the U10Mo and U10Mo1Zr samples, higher Zr content would also promote the completion of the reaction. Unfortunately there is no data on the specific change in reaction order in higher Zr content alloys.

Characterization Techniques

XRD

X-rays are a form of high-energy electromagnetic radiation that can have energies

ranging from 200 eV to 1MeV. X-rays are a result of the interaction between an incident electron

beam and the electrons that comprise the shell of an atom. Typical interatomic spacing is in the

range of 2 angstroms which puts the useful wavelengths for x-rays between .5 and 2.5 angstroms.

Considering typical interatomic spacing, accelerating potentials on the range of 10kV are

utilized. To produce x-rays a tube comprising of two metal electrodes in a vacuum chamber are

biased so that electrons are produced and travel from cathode (source, usually a tungsten

filament) to anode. Due to the production of multiple wavelengths from a given source and the

potential of excitation from multiple shells around an atom, a monochromator is regularly used

in order to limit the x-rays to one wavelength. Incident electrons that carry sufficient energy to

remove an inner shell electron produce an electron hole. When recombination involving an

electron from the outer shell and the aforementioned hole occurs, a characteristic x-ray photon is

produced [28].

When x-rays are diffracted in phase, and constructively, from a sample, a relatively

higher signal reaches the detector and a peak is produced in the XRD pattern. Due to the multiple

peaks produced by a phase in a sample caused by multiple diffracting planes in a material, a

characteristic pattern is produced for any given material. Multiple phases in a sample all produce

their own characteristic pattern. The resultant pattern produced can contain overlapping peaks

due to similar lattice characteristics as well broadening of the peaks due to small crystallite sizes

and strain in the lattice This pattern can then be identified and quantified using deconvolution and various techniques in order to obtain the identity and relative amounts of phases present [28].

Powder mixture quantitative analysis was used to analyze the alloys of interest. Intensity and location of a given peak depend on the phase content present and lattice parameter respectively. Using a JCPDS card catalogue peak locations and relative intensities can be determined and used to identify phases present as well as relative phase content in the mixture. Relations between the content and diffracted intensity are not linear. This relationship depends primarily on the absorption coefficient of the phase of interest in the mixture. There are a few well known methods of extracting quantitative peak intensity data from XRD patterns. All of which are dependent on the absorption coefficient on the mixture. Identical XRD conditions are necessary in generating any results involved in these methods. The following descriptions pertain to a mixture of only two phases [28].

External Standard Method

The external standard method involves knowing the mass absorption coefficients of both phases of interest and being able to find the intensity of a given peak from a pure phase sample. By seeing how the intensity changes from the pure peak to the mixture, a weight fraction of that phase in the mixture can be determined. If however, there are not mass absorption coefficients available for the phases of interest, a calibration curve can be used to determine how the peak intensity changes from pure phase to mixture given that the calibration curve is generated from a mixture of known composition [28].

Direct Comparison Method

The direct comparison method involves using the structure of the phases of interest, diffracted angle, and respective peak identity (hkl). One can find the relative intensity of the two phases and knowing the structure, determine a ratio of concentrations. This method requires that the observed peaks are used to calculate the structural information. It also requires that the peaks of two phases not be overlapping as it changes both the structural information calculated from the pattern as well as the integrated intensity determined [28].

Internal Standard Method

This method pertains only to powders and involves mixing a known weight fraction of a substance into the mixture and then using the intensity ratios of the phase of interest and the substance to find the content of the phase of interest in the sample. A calibration curve can be generated and then used to determine the weight fraction of the phase of interest after mixing a known amount of substance into the sample mixture. This method requires powders and requires a separate standard determined by the introduction of the substance for each phase of interest in the mixture [28].

SEM

Scanning electron microscopy involves the production of electrons under vacuum in the range of 1-40 KeV and subsequent focusing of the electron beam using a series of electromagnetic lenses in order to focus the electron beam onto the surface of the sample. After

the beam hits the surface of a sample, many different signals are generated and a detector is used to collect relevant data.

Backscatter and Secondary Electrons

Typically secondary electrons and backscattered electrons are used to obtain topographical and atomic number/compositional contrast data respectively. The relative amount of secondary electrons that escape a surface depends on the edge effect. More electrons escape edges compared to flat surfaces and in effect generate a topographical map of the surface of interest. Backscattered electrons are a result of multiple elastic collisions inside the interaction volume of the electron beam with the sample. When collisions occur in a way that allow the electrons to escape the surface of the sample, a detector can pick up the signal. The variation in energies back scattered associated with the difference in atomic number can then be used to produce an image which provides valuable compositional information [29].

XEDS

The electron beam interaction volume also produces characteristic x-rays. The x-rays produced are characteristic of the atoms present. By using these characteristic x-rays, compositional data can be generated and used to determine relative weight or atomic percentages of the atoms present at a point, in a line, or in the area of interest of the sample [29].

CHAPTER 3: EXPERIMENTAL METHOD

U10Mo+Zr ALLOYS

The U10MoZr alloys were obtained via collaboration with Idaho National Labs. The alloys varied in weight percent (0, 0.5, 1, 2, 5, 10, and 20 wt.% Zr) and they were all fabricated by induction melting in a graphite crucible.

Heat Treatments and Encapsulation

Before each heat treatment, the sample of interest was encapsulated in a quartz tube containing a 1.0 cm^2 piece of tantalum foil acting as an oxygen getter to minimize the oxidation. The quartz tube was then purged using a roughing pump to an internal pressure of 1-3 atm and subsequently vacuumed to 1.0×10^{-6} atm. These pressures were used in each and every purge step in this experiment. The quartz tube was then backfilled with hydrogen to an internal pressure of 550-650 torr, this pressure was used for every backfilling step in this experiment. The tube was then subsequently purged of hydrogen. Following the hydrogen backfill and purge, a series of three argon backfills and purges were utilized to ensure low oxygen content inside the quartz tube. After the purging steps, a final high vacuum step down to 1.0 X 10^{-6} atm was obtained and the capsule was sealed. Figure 15 shows the encapsulation system which includes an acetylene torch and a series of pumps to backfill the tubes and purge the gaseous contents.

Figure 15 Encapsulation system: acetylene torch(left) and vacuum system(right).

Figure 16 shows the Lindberg Blue M Three-Zone Tube Furnace used for all heat treatments. Figure 17 shows the diamond saw used for sample sectioning as well as the Ar filled glove box used in sample preparation.

Figure 16 Lindberg Blue M Three-Zone tube furnace used in heat treatments

Figure 17 Diamond saw(left) and Ar glovebox(right)

Upon receiving the alloys, all 7 rods (U10Mo + 0 wt.% Zr, 0.5 wt.% Zr, 1 wt.% Zr, 2 wt.% Zr, 5 wt.% Zr, 10 wt.% Zr, and 20 wt.% Zr) were homogenized at 900°C for 7 days and water quenched by submerging the heated quartz tube in water and breaking the tube using a hammer. The 7 rods were then sectioned into 1mm thick. A few discs of each composition were taken out of the sample population, and then labeled 900˚C water quenched for x-ray diffraction, scanning electron microscopy, and energy dispersive spectroscopy. After homogenization, a set of discs from each alloy were then encapsulated individually and heated at 650°C for 3 hours.

Sample Mounting and Polishing

The samples were then mounted in epoxy was left to cure overnight. The samples were then prepared for standard metallographic polishing using a Minimet auto-polisher shown in Figure 18. The polishing included the following steps using an oil lubricant: 240 grit SiC paper to remove the epoxy and expose the surface of each alloy, 600 grit SiC paper, 800 grit SiC paper, and finally 1um diamond paste. Between each polishing step, the sample was ultrasonicated in acetone and then rinsed with ethanol.
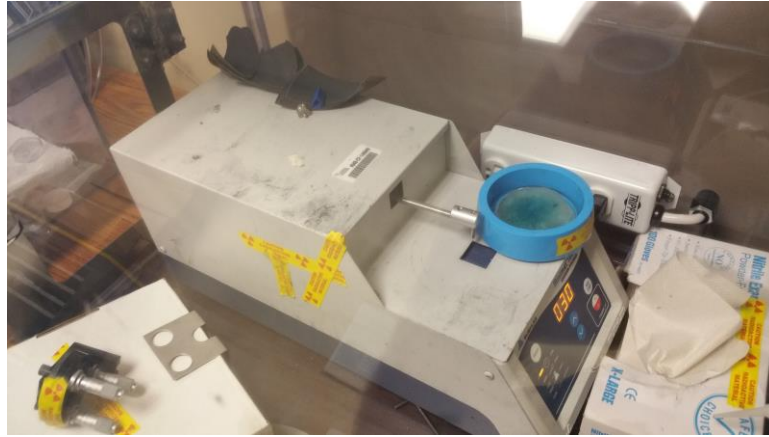
Figure 18 Minimet auto-polisher

Analysis of the Samples

The polished samples were then examined in a Zeiss scanning electron microscope (SEM) equipped with energy dispersive spectroscopy (EDS). Each sample had a series of images taken at various magnifications. These images were later used for an image analysis technique that resulted in a cursory phase weight fraction for each alloy and heat treatment. EDS was utilized to semi-quantitatively verify some of the phase identities. XRD was also utilized in order to bolster image analysis and lever rule results.

Ternary Diagram Analysis and Calculations

A lever rule technique outlined below, predicted weight percentages of each phase present in each alloy were determined using the labeled alloy compositions. The technique, depicted in Figure 19, involved drawing a line from the Mo_2Zr composition through the composition of the alloy, marked as a red dot, and ending on the γ-U phase of the ternary phase diagram. The techniques used, also enabled the determination of the atomic masses and densities

of each γ-U composition formed during the 900˚C homogenization heat treatment for each alloy present in this study.
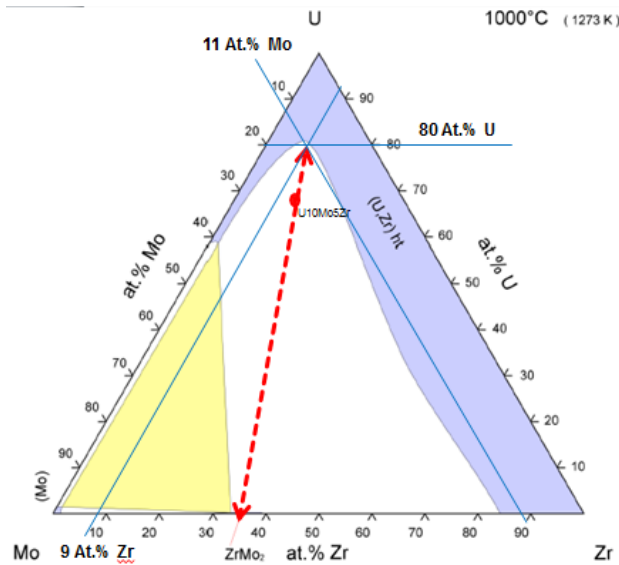
Figure 19 Lever rule depiction used calculate γ-U phase density

Density of the γ-U phase for each alloy, (ρ_γ), was determined by taking the atomic fraction and weight of the constituent elements, A_{fe} and A_{we} respectively, to determine the weight of each constituent element W_e present in the alloy of interest, seen in Equation 1. Atomic weights for each element are presented in Table 3. Atomic fraction of each element was determined from the ternary phase diagram as indicated in Figure 19.

$$W_e = A_{fe}A_{we} \hspace{6cm} (1)$$

Table 3 Atomic weights and densities of constituent elements for use in determining densities of the γ-U phase

Element	Standard Atomic Weight(g/mol)(A_{we})[30]	Density(g/cm^3)(ρ_e)
U	238.03	19.1[25]
Mo	95.95	10.2[31]
Zr	91.22	6.52[32]

Conversion of the W_e to a weight fraction of the elements present in the γ-U phase (W_{fe}) using the total atomic mass, or the sum of the weights of the elements in the γ-U phase at that composition can be seen in Equation 2.

$$w_{fe} = \frac{w_e}{\sum w_e}$$

(2)

Using W_{fe} and the respective density of each constituent element (ρ_e) shown in Table 3, a weighted average of the constituent element densities was used to determine the ρ_γ for each alloy, presented in Equation 3. γ-U densities and atomic weights determined from the 1000˚C ternary phase diagram for each alloy after a 900˚C homogenization are presented in Table 4. These densities are later used in image analysis.

$$\rho_\gamma = \sum W_{fe}\rho_e$$

(3)

Table 4 Densities and total atomic weights for the γ-U phase organized by Zr concentration after a 900˚C heat treatment

Alloy	γ Phase Total Atomic Weight(g/mol)(W_p)	γ Phase Density(g/cm^3)(ρ_p)
U10Mo	207.38	18.22
U10Mo0.5Zr	209.35	18.28
U10MoZr	203.75	18.06
U10Mo2Zr	204.33	18.04
U10Mo5Zr	209.19	18.16
U10Mo10Zr	197.49	17.66
U10Mo20Zr	165.57	15.99

Equation 4 depicts how the atomic fraction of the phase, A_{fp}, is determined using a lever rule with d_p referring to the length on the lever opposite to the phase of interest.

$$A_{fp} = \frac{d_p}{\Sigma d_p}$$ (4)

The atomic fraction of the phase is then used with the atomic weight of that particular phase, A_{wp} to find the respective weight of the phase in the alloy, W_p, as seen in Equation 5. Atomic weights of each phase, A_{wp} are presented in Table 5.

$$W_p = A_{wp}A_{fp}$$ (5)

Table 5 Atomic weights and densities of phases predicted from the ternary phase diagrams in this study

Phase	Density(g/cm^3)(ρ_p)[25]	Atomic Weight(g/mol)(A_{wp})
γ-U	See Table 4	See Table 4
α-U	19.1	238.03
Mo$_2$Zr	8.57	94.28
U$_2$Mo	16.45	188.76

The weights of the phases are then used in Equation 6 to determine a predicted lever rule weight percent, $L\%_p$, of the phase in the alloy of interest after a given heat treatment.

$$L\%_p = 100 \times \frac{W_p}{\Sigma W_p} \qquad\qquad (6)$$

Image Analysis

Using program called ImageJ, the back scattered images of the samples were analyzed. To do so, the contrasts of the images were adjusted and each phase was isolated. The difference in atomic number of each phase allowed for a clear distinction of each phase due to their varying contrast levels in backscatter mode from the SEM. Figure 20 shows how ImageJ was utilized for the U10Mo10Zr sample after a 650˚C heat treatment for 3 hours followed by water quenching. Note that first Mo_2Zr area% was found followed by γ-U. The remaining area% was assumed to be α-U.

(A)   (B)   (C)
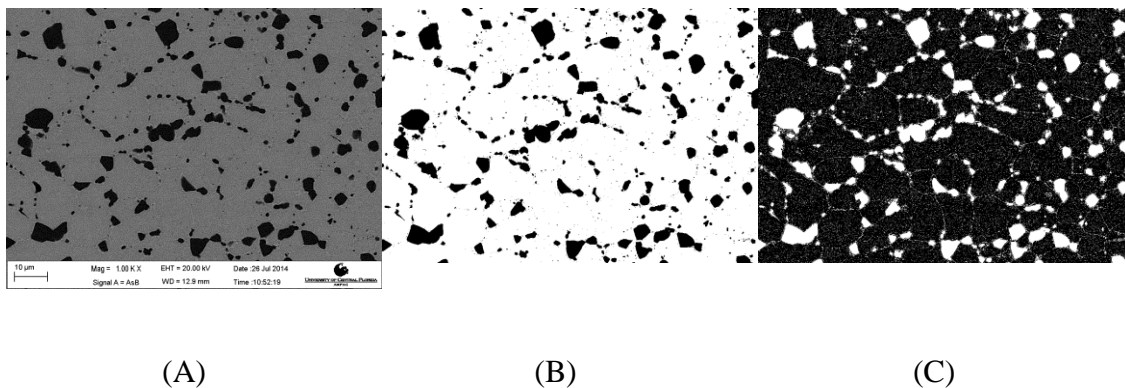
Figure 20 ImageJ process example using U10Mo10Zr after a 650˚C heat treatment for 3 hours followed by a water quench (a) original backscatter electron micrograph (b) image showing Mo_2Zr after image processing (c) image showing γ-U after image processing

Using the area percentages obtained in ImageJ as well as the densities of the phases presented by Ivanov, ρ_p, [25], weight percent of each phase as determined by image analysis was found. This was done under the assumption that the area fraction observed from the back scattered SEM micrographs were equivalent to the volume fraction of the phases present in the sample of interest. The weight of the phase present in the image, I_p was determined by multiplying the volume fraction of the phase determined by image analysis, V_{fp} by the density of that phase (ρ_p) shown in Equation 7.

$$I_p = (V_{fp})(\rho_p) \tag{7}$$

Image weight percent of a phase of interest, $I\%_p$ was then calculated by using Equation 8.

$$I\%_p = 100 \times \frac{I_p}{\sum I_p} \tag{8}$$

XRD Integrated Intensity Analysis

X-Ray Diffraction was used to quantitatively analyze the phases present. Patterns generated from XRD were then deconvoluted and analyzed using integrated intensities. To generate integrated intensities, Origin was used to find the integrated intensity of one peak (preferably stand-alone) and then using relative intensity ratios from the JCPDS files, the remaining relative intensities for the phase of interest were calculated assuming no texturing. The total integrated intensity of the phase of interest, p, was then summed and called integrated intensity of phase p (N_p). By dividing N_p by the total integrated intensity under the curve, or the sum of all the I_p for every phase, a relative amount of phase p in the sample was determined (R_p) shown in Equation 9.

$$R_p = 100 \times \frac{N_p}{\sum N_p} \qquad\qquad (9)$$

CHAPTER 4: RESULTS AND ANALYSIS

In each section organized by composition, two ternary diagrams will be presented representing phases present after heat treatments of 900˚C for 168 hours and 650˚C for 3 hours, with the composition of the sample marked by a red circle. Expected phases will be presented based on the ternary phase diagrams and the phases observed are presented based on XRD and image analysis. Back scattered micrographs and XRD patterns of the sample of interest will be presented as well. Weight percentages predicted by the lever rule and image analysis results will then be compared to the observations from the integrated intensities.

U10Mo + 0 wt.% Zr

Both phase diagrams in Figure 21 predict the composition to lie in a γ-U region. The lack of Zr in the sample prevents any Mo_2Zr from forming and high temperatures prevent γ to α decomposition from occurring as seen in the micrographs presented in Figure 22 and Figure 23. Figure 24 shows the XRD patterns of the U10Mo samples after a 900˚C homogenization step as well as a 650˚C heat treatment for 168 and 3 hours respectively. From Figure 24 and the resultant integrated intensity results presented in Table 6, it is clear that only -U is present in the U10Mo samples after both heat treatments. Table 7 presents the expected phases as determined by the ternary diagram as well as the observed phases from the XRD patterns and micrographs. Image, lever, and integrated intensity analysis all agree that this sample contains 100% γ-U.

Figure 21 1000°C and 650°C U-Mo-Zr phase diagrams with U10Mo+0 wt.% Zr composition labeled

Figure 22 U10Mo0Zr backscattered micrograph after a 900°C heat treatment for 168 hours

Figure 23 U10Mo0Zr backscattered micrograph after a 650˚C heat treatment for 3 hours
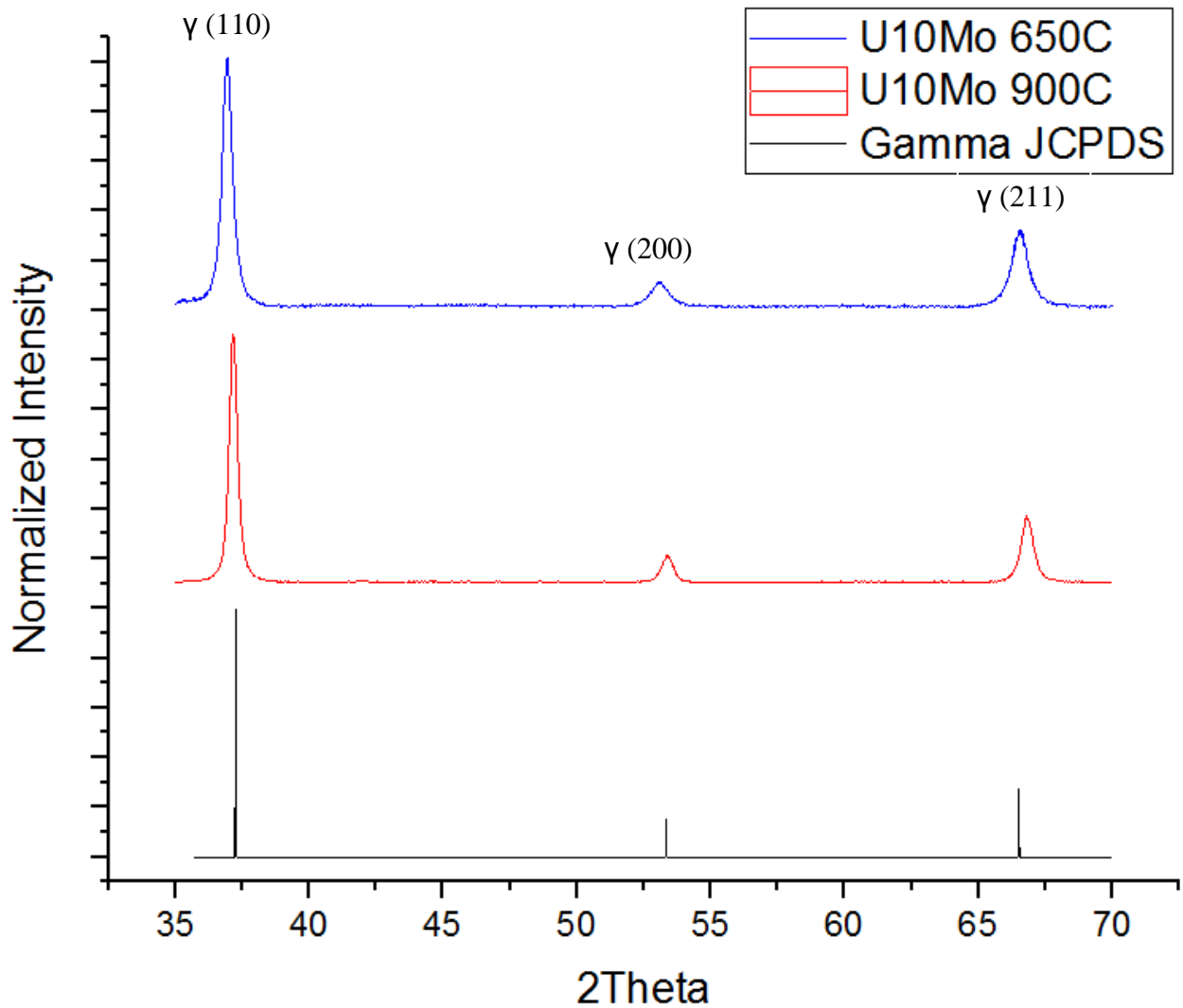
Figure 24 XRD pattern for U10Mo0Zr after 900˚C and 650˚C heat treatments

Table 6 Lever rule, image analysis, and integrated intensity results for U10Mo0Zr after 900˚C and 650˚C heat treatments

Sample	Lever Rule	Image Analysis	Integrated Intensity
U10Mo0Zr 900˚C	100% γ-U	100% γ-U	100% γ-U
U10Mo0Zr 650˚C	100% γ-U	100% γ-U	100% γ-U

Table 7 Expected and observed phases in the U10Mo0Zr sample after 900˚C and 650˚C heat treatments

Heat Treatment for U10Mo	Expected Phases from Ternary Phase Diagram	Observed Phases
900˚C Water Quenched	γ-U	γ-U
650˚C Water Quenched	γ-U	γ-U

U10Mo + 0.5 wt.% Zr

Both phase diagrams in Figure 25 predict that the U10Mo0.5Zr composition lies in a one phase region containing only γ-U after the 900˚C homogenization step and the subsequent 3 hour 650˚C heat treatment. In the micrographs shown in Figure 26 and Figure 27, small Zr rich regions can be seen as verified by the XEDS data shown in Figure 28. Figure 29 shows the XRD patterns generated from the U10Mo0.5Zr sample after a 650˚C 3 hour heat treatment. Both the XRD pattern and integrated intensity data presented in Table 8 demonstrate the presence of only the γ-U phase, however a Zr rich phase is observed in the backscatter micrographs. Predicted phases from the two ternary phase diagrams as well as the observed phases from XRD and the backscattered micrographs are presented in Table 9. Image analysis, lever rule, and the integrated intensity results support that, once again a lack of sufficient Zr prevents Mo_2Zr from forming. The sample contains 2 phases, γ-U with regions of higher Zr content.
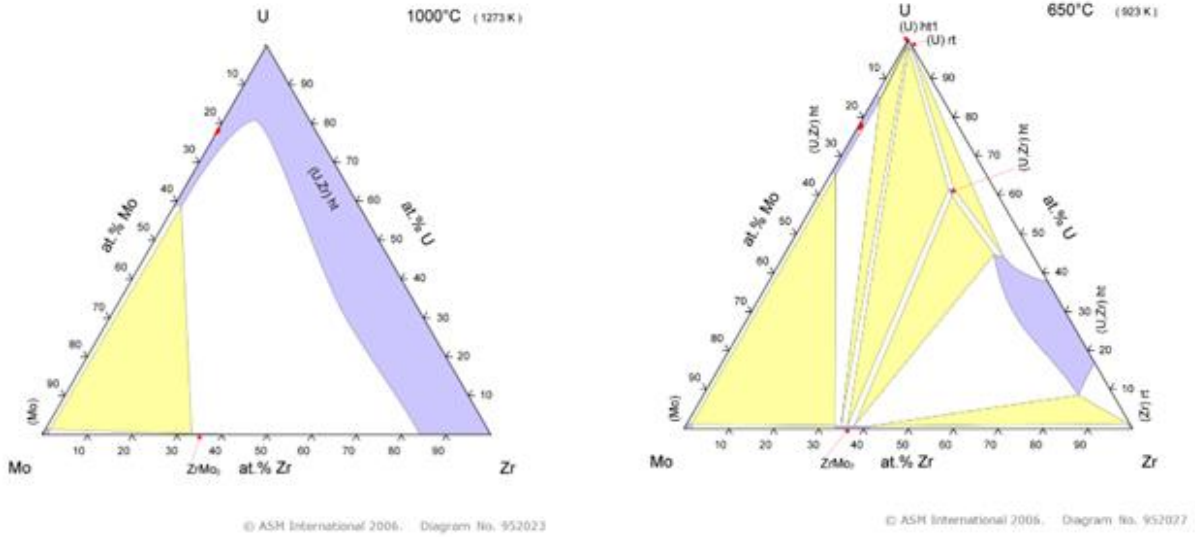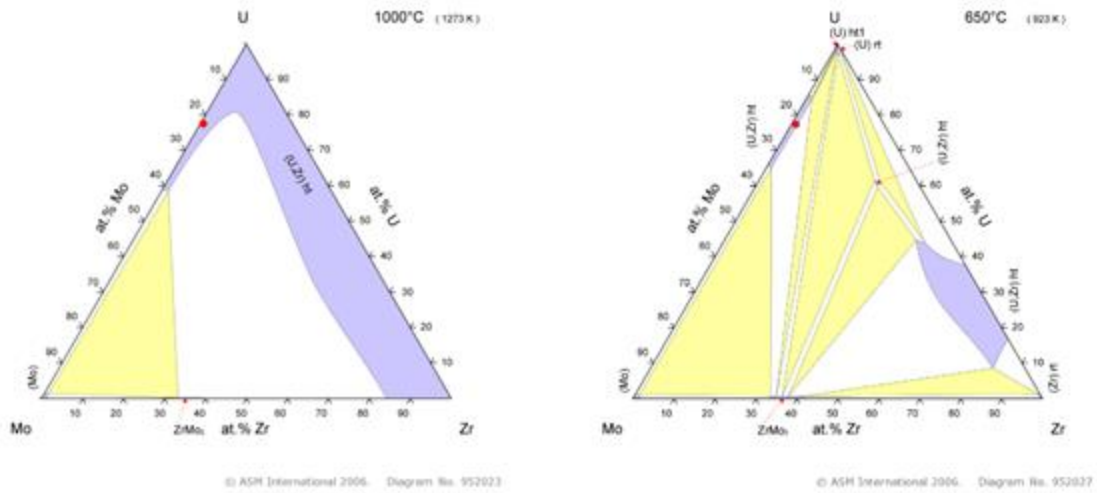
Figure 25 1000˚C and 650˚C U-Mo-Zr phase diagrams with U10Mo+0.5 wt.% Zr composition labeled
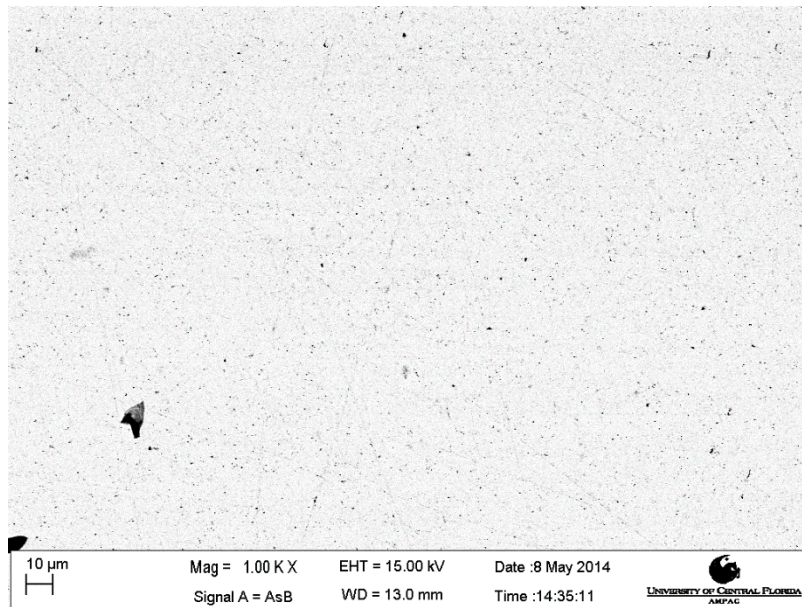

Figure 26 U10Mo0.5Zr backscattered micrograph after a 900˚C heat treatment for 168 hours
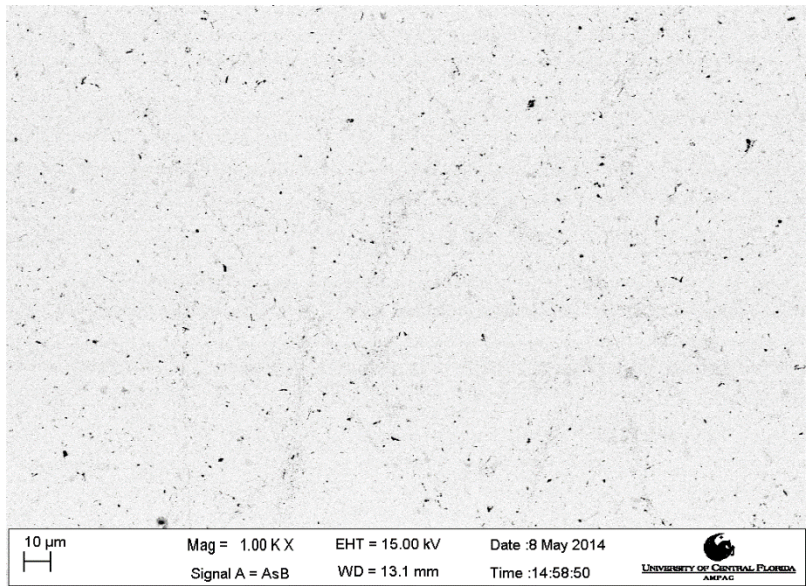
Figure 27 U10Mo0.5Zr backscattered micrograph after a 650˚C heat treatment for 3 hours

Full scale counts: 1363   Base(2)_pt2
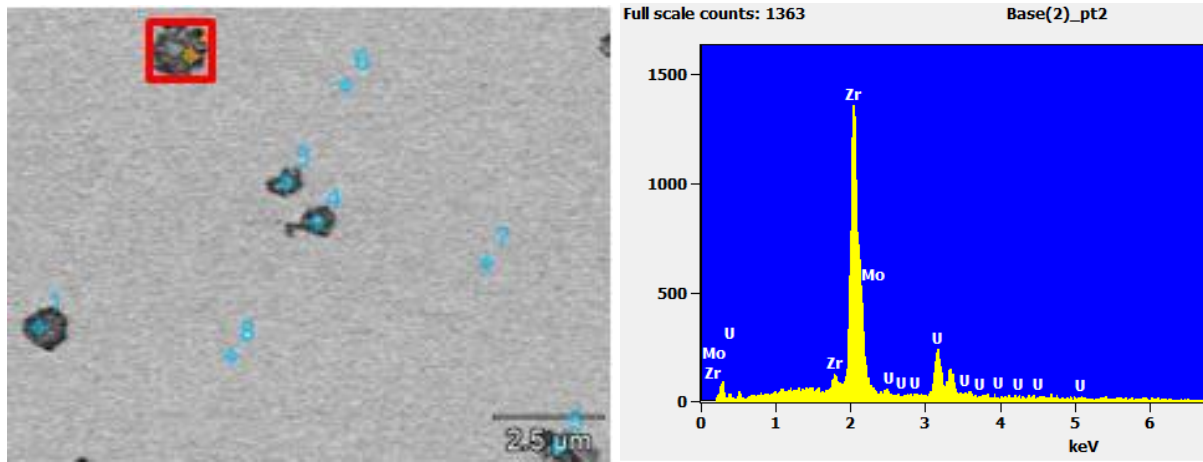
(A)   (B)

Wed Jun 04 10:57:13 2014
Filter Fit   Chi-squared value: 1.204   Errors:+/-1 Sigma
Correction Method: ZAF
Acc.Voltage: 15.0 kV   Take Off Angle: 35.0 deg

Element	Element Wt.%	Wt.% Error	Atom %
Zr	65.71	+/-1.08	82.76
Mo	0.97	+/-0.62	1.16
U	33.32	+/-1.91	16.09
Total	100.00		100.00

(C)

Figure 28 XEDS data for the U10Mo0.5Zr sample after a 650˚C heat treatment for 3 hours (A) micrograph of the selected area (B) XEDS pattern generated by the dark phase formed after a 3 hour heat treatment at 650˚C (C) XEDS compositional data generated by the dark precipitate in the U10Mo0.5Zr sample after a 650˚C heat treatment for 3 hours
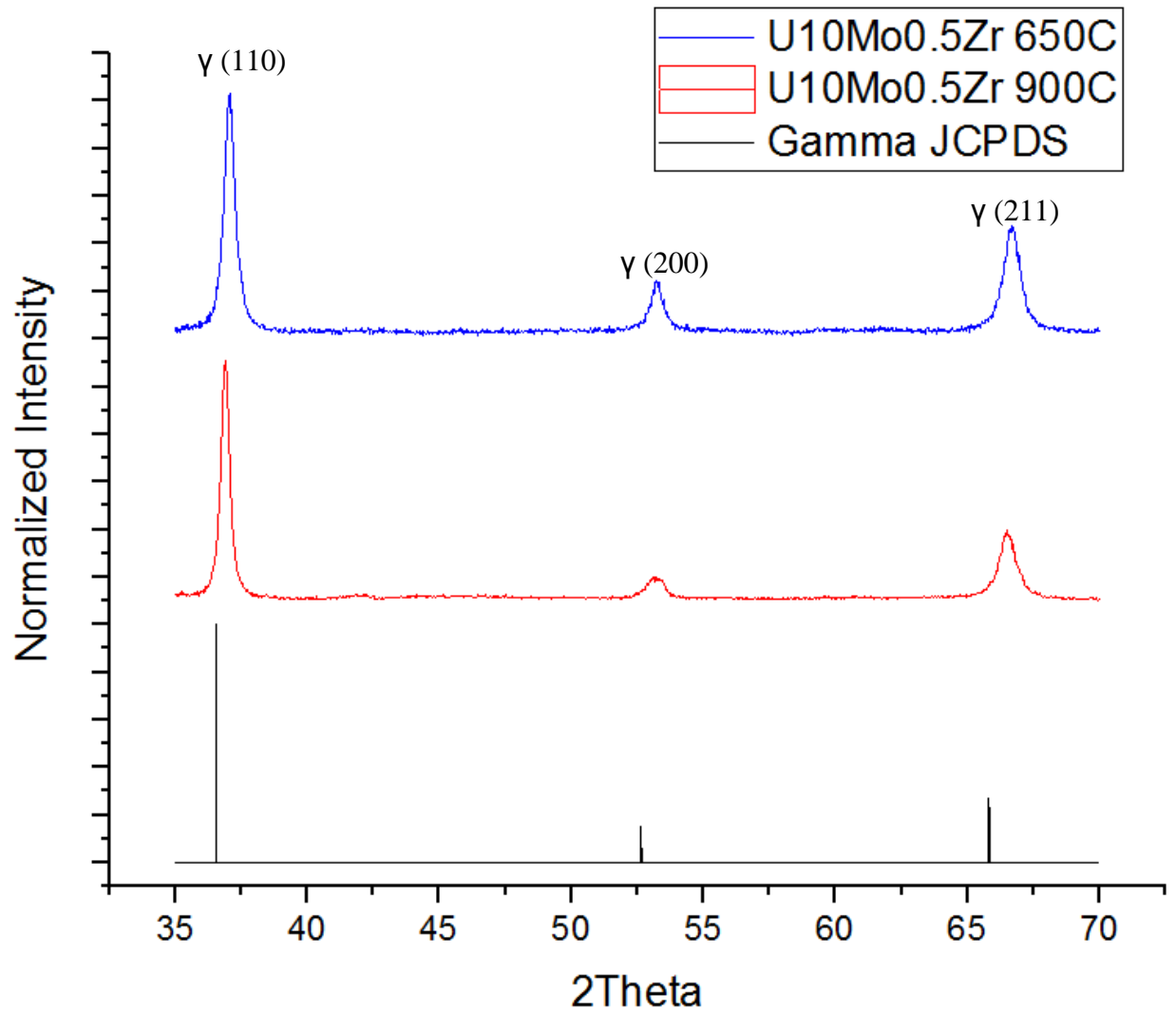
Figure 29 XRD patterns for U10Mo0.5Zr after 900°C and 650°C heat treatments

Table 8 Lever rule, image analysis, and integrated intensity results for U10Mo0.5Zr after 900°C and 650°C heat treatments

Sample	Lever Rule	Image Analysis	Integrated Intensity
U10Mo0.5Zr 900°C	100% γ-U	99.7% γ-U 0.30% Zr Rich Phase	100% γ-U
U10Mo0.5Zr 650°C	100% γ-U	99.6% γ-U 0.40% Zr Rich Phase	100% γ-U

Table 9 Expected and observed phases in the U10Mo0.5Zr sample after 900˚C and 650˚C heat treatments

Heat Treatment for U10Mo0.5Zr	Expected Phases from Ternary Phase Diagram	Observed Phases
900˚C Water Quenched	γ-U	γ-U
650˚C Water Quenched	γ-U	γ-U

U10Mo + 1 wt.% Zr

The ternary phase diagrams in Figure 30 predict a one phase γ-U structure after the 900˚C homogenization and subsequent 3 hour 650˚C heat treatment. Micrographs in Figures 31 and Figure 32 depict a two phase region with the presence of Zr rich precipitates in a γ-U matrix. The XRD pattern from Figure 33 as well as the integrated intensity data from Table 10 shows the presence of only γ-U. Table 11 shows that the predicted phase from the ternary diagrams as well as the observed phases from XRD, both of which only demonstrate a one phase region of γ-U. Lack of sufficient Zr prevents Mo_2Zr nucleation and the subsequent γ-U destabilization that can follow. Lever rule, image analysis, and integrated intensity all verify that the γ-U phase is present, however the image analysis indicates that a Zr rich phase is forming.

Figure 30 1000˚C and 650˚C U-Mo-Zr phase diagram with U10Mo+1 wt.% Zr composition labeled

45
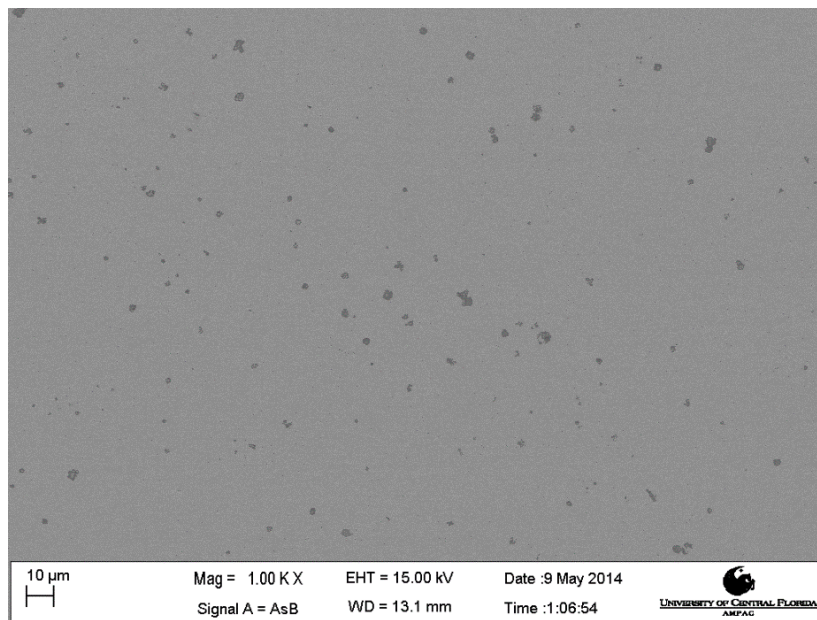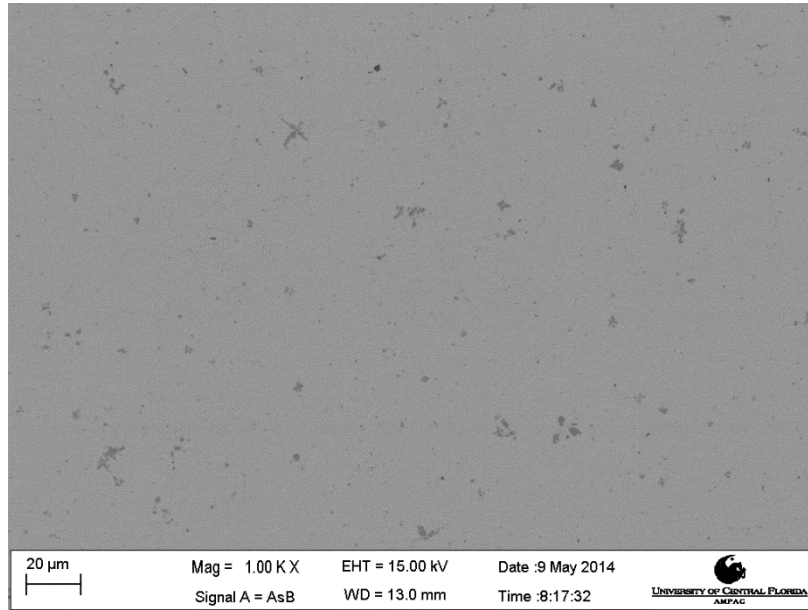
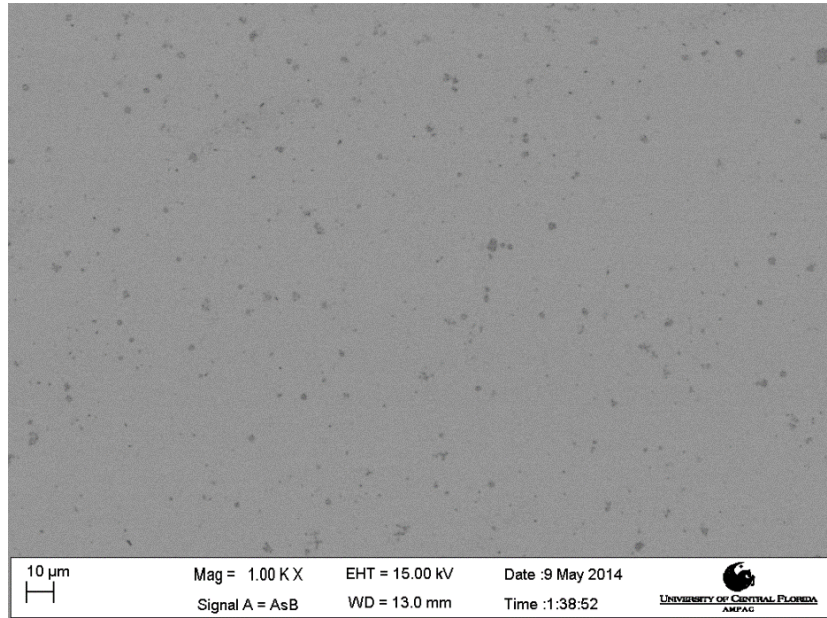Figure 31 U10Mo1Zr backscattered micrograph after a 900˚C heat treatment for 168 hours

Figure 32 U10Mo1Zr backscattered micrograph after a 650˚C heat treatment for 3 hours
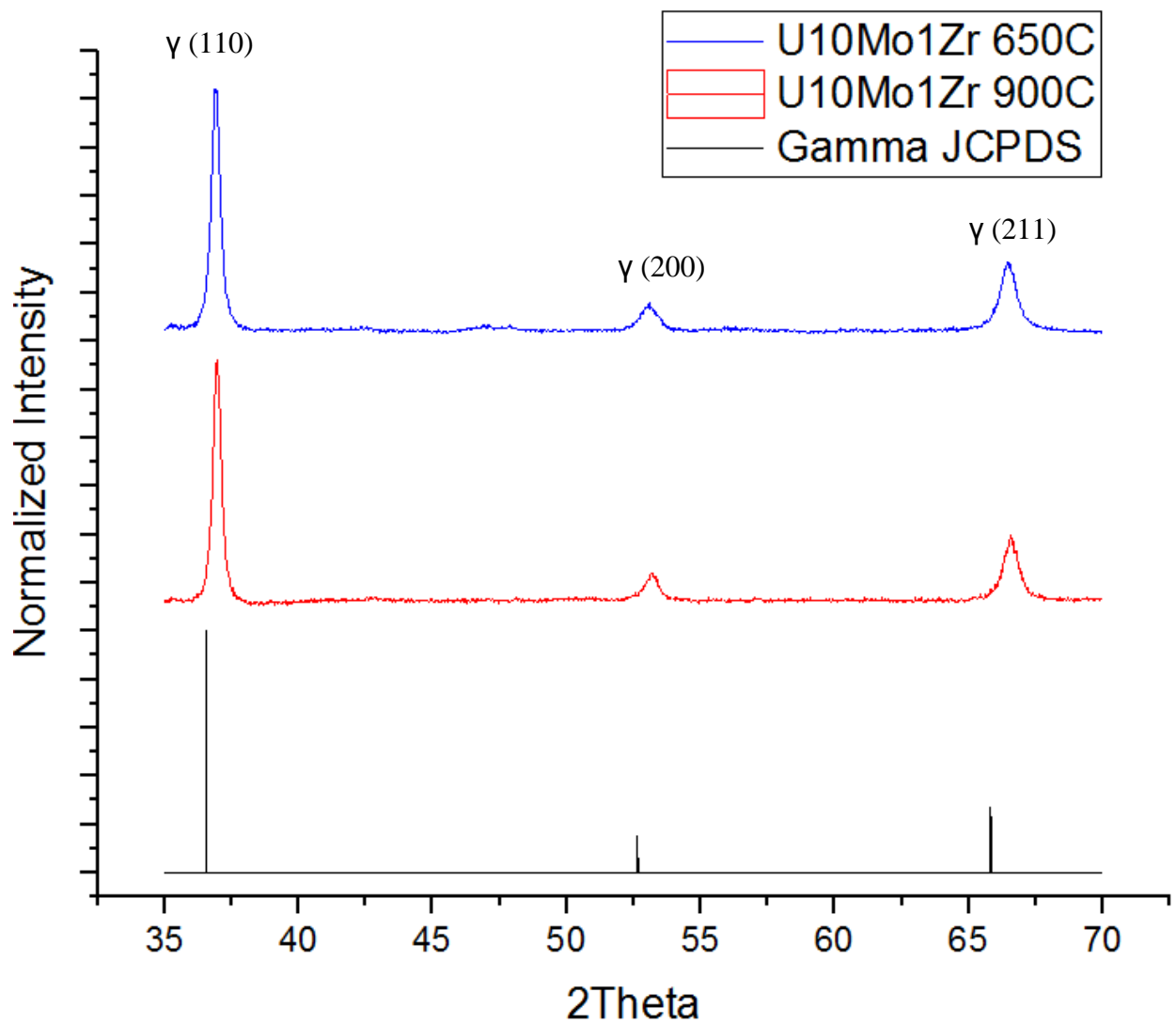
Figure 33 XRD pattern for U10Mo1Zr after 900˚C and 650˚C heat treatments

Table 10 Lever rule, image analysis, and integrated intensity results for U10Mo1Zr after 900˚C and 650˚C heat treatments

Sample	Lever Rule	Image Analysis	Integrated Intensity
U10Mo1Zr 900˚C	100% γ-U	99.4% γ-U 0.60% Zr Rich Phase	100% γ-U
U10Mo1Zr 650˚C	100% γ-U	99.3% γ-U 0.70% Zr Rich Phase	100% γ-U

Table 11 Expected and observed phases in the U10Mo1Zr sample after 900˚C and 650˚C heat treatment

Heat Treatment for U10Mo1Zr	Expected Phases from Ternary Phase Diagram	Observed Phases
900˚C Water Quenched	γ-U	γ-U
650˚C Water Quenched	γ-U	γ-U

<u>U10Mo + 2 wt.% Zr</u>

From the ternary phase diagrams shown in Figure 34, a two phase region of γ-U and Mo_2Zr is predicted in the U10Mo2Zr sample after both heat treatments at 900˚C and 650˚C. The micrographs in Figure 35 and Figure 36 show a Mo_2Zr phase forming at the grain boundaries of γ-U. XEDS data presented in Figure 37 shows that the composition of the phase at the grain boundaries is in fact Mo_2Zr. XRD from Figure 38 shows representative γ-U peaks as well as small peaks resembling Mo_2Zr at around $2\theta=39$˚ and $2\theta=41$˚. The integrated intensity data displayed in Table 12 shows that Mo_2Zr content increases after a 650˚C heat treatment for 3 hours. Table 13 shows that the predicted phases from the ternary phase diagrams as well as the observed phases from XRD and image analysis indicate the presence of both Mo_2Zr and γ-U. At 2 wt.% Zr, there is sufficient Zr present to start the formation of Mo_2Zr given the time allowed for reaction. These Mo_2Zr precipitates are seen forming both inside the grains and at the grain boundaries of γ-U. The image analysis suggests no increase in Mo_2Zr wt.% however, both the lever rule and the integrated intensity analysis indicate an increase in Mo_2Zr presence after the

48

650˚C heat treatment. No α-U is predicted nor observed in this sample. Not enough Mo depletion has occurred from the γ-U phase to allow this destabilization and subsequent γ-U transformation into α-U to occur.
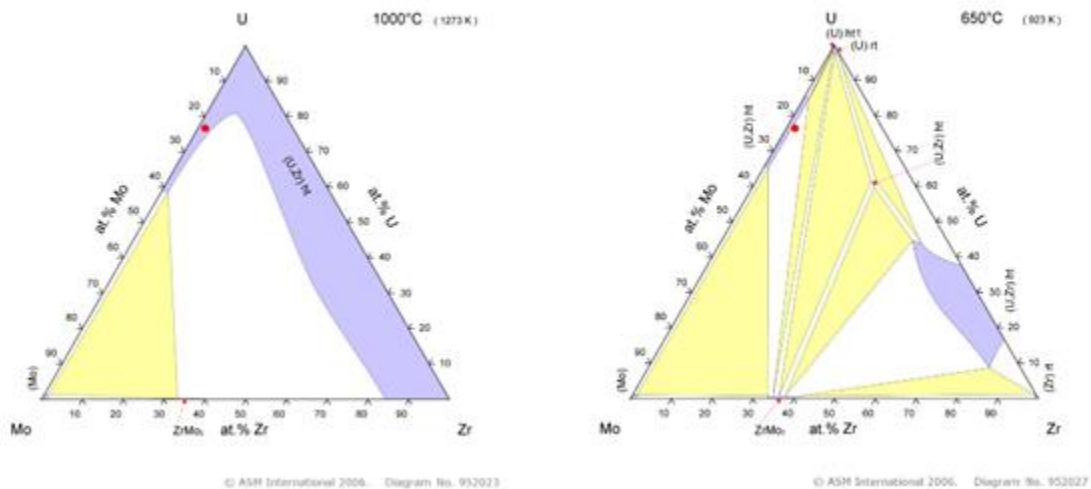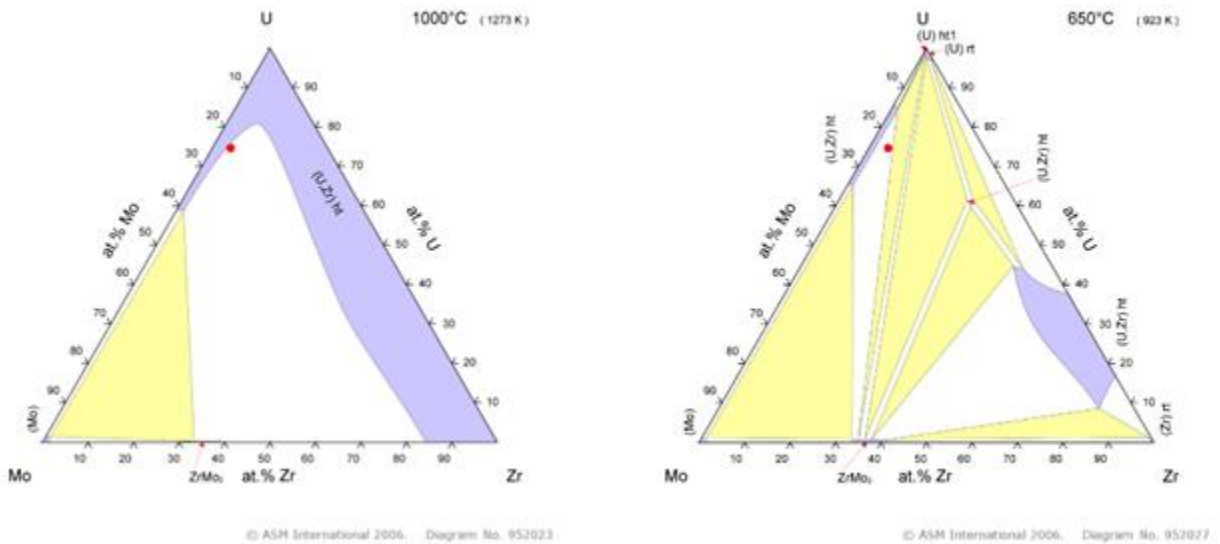

Figure 34 1000˚C and 650˚C U-Mo-Zr phase diagram with U10Mo+2 wt.% Zr compositions labeled
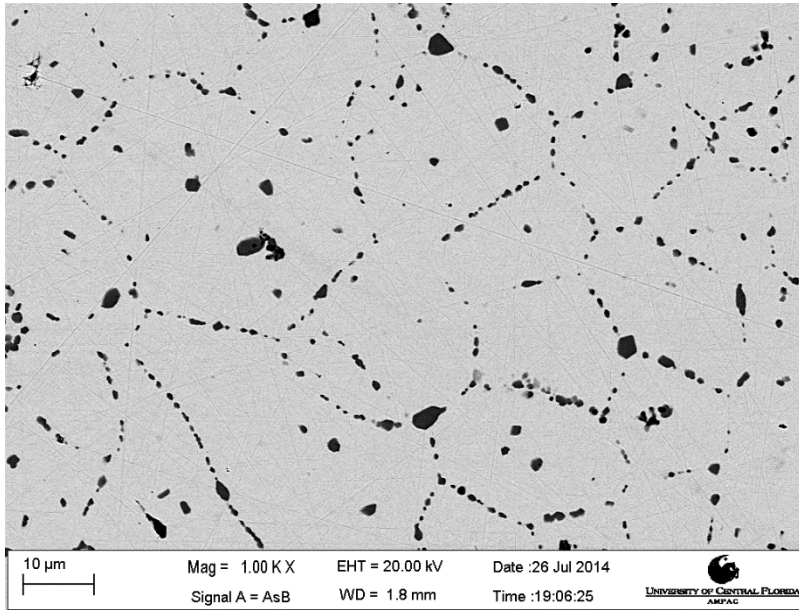
Figure 35 U10Mo2Zr backscattered micrograph after a 900˚C heat treatment for 168 hours
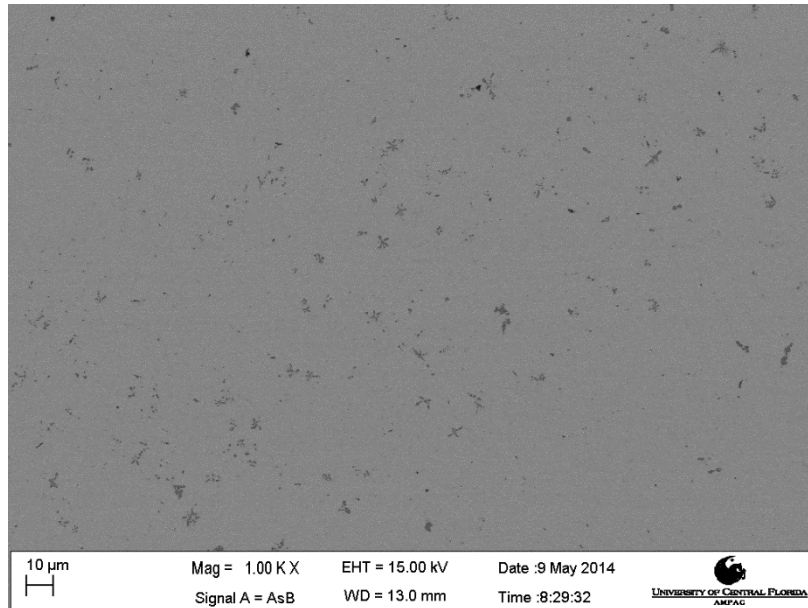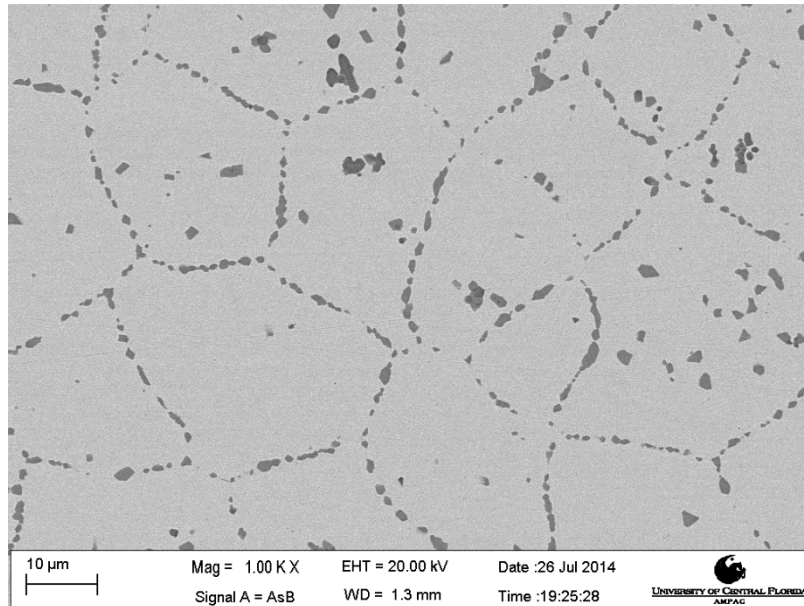

Figure 36 U10Mo2Zr backscattered micrograph after a 650˚C heat treatment for 3 hours
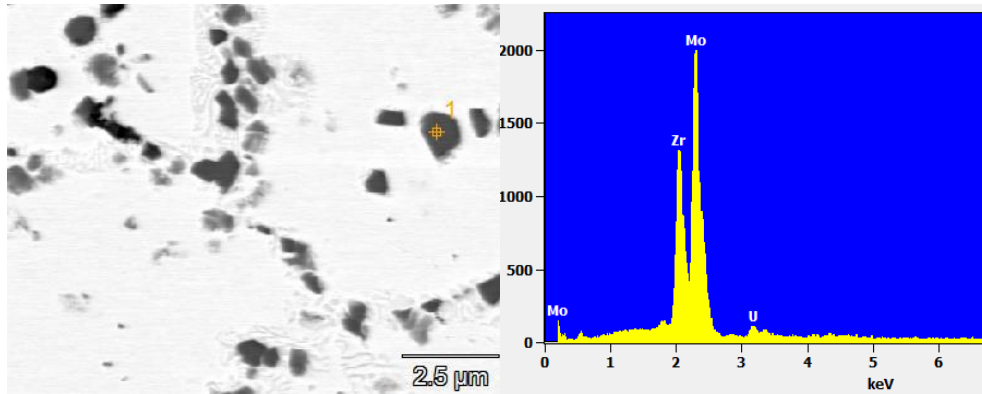
(A)   (B)

```
Thu Oct 22 22:16:08 2015
Filter Fit   Chi-squared value:  6.094   Errors:+/-1 Sigma
Correction Method:  ZAF
Acc.Voltage: 20.0 kV  Take Off Angle: 35.0 deg

Element         Element        Wt.%          Atom %
                Wt.%           Error
  Zr            30.29          +/-0.62        32.91
  Mo            61.72          +/-0.96        63.76
  U              7.98          +/-0.54         3.32
                ----------                    ----------
Total          100.00                        100.00
```

(C)

Figure 37 XEDS data for the U10Mo2Zr sample after a 650°C heat treatment for 3 hours (A) micrograph of the selected area (B) XEDS pattern generated by the dark precipitate in the U10Mo2Zr sample after a 650°C heat treatment for 3 hours (C) XEDS compositional data

51
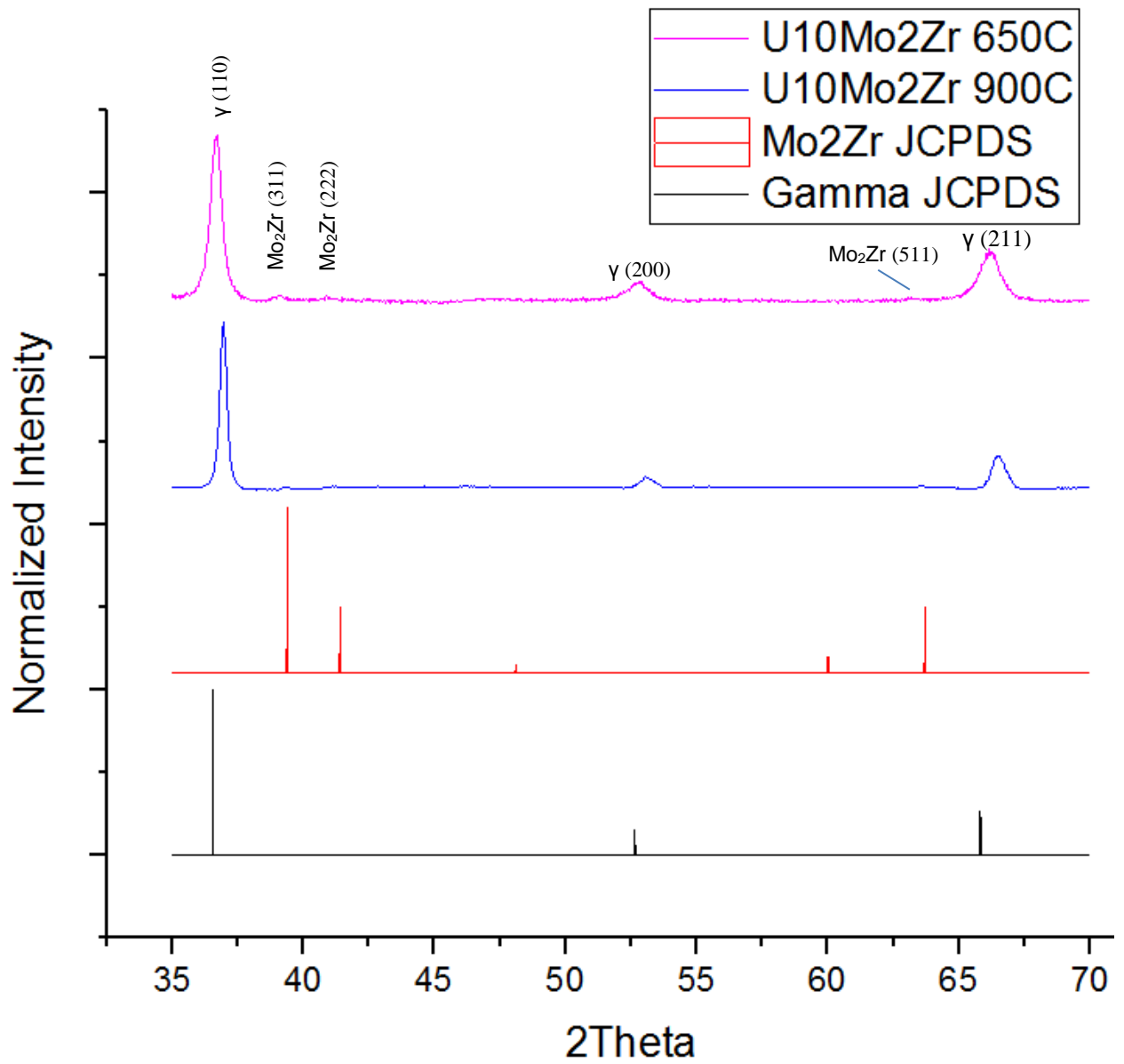
Figure 38 XRD pattern for U10Mo2Zr after 900˚C and 650˚C heat treatments

Table 12 Lever rule, image analysis, and integrated intensity results for U10Mo2Zr after 900˚C and 650˚C heat treatments

Sample	Lever Rule	Image Analysis	Integrated Intensity
U10Mo2Zr 900˚C	98.9% γ-U 1.1% Mo$_2$Zr	97.5% γ-U 2.5% Mo$_2$Zr	97.8% γ-U 2.2% Mo$_2$Zr
U10Mo2Zr 650˚C	95.9% γ-U 4.1% Mo$_2$Zr	97.5% γ-U 2.5% Mo$_2$Zr	96.3% γ-U 3.7% Mo$_2$Zr

Table 13 Expected and observed phases in the U10Mo2Zr sample after 900˚C and 650˚C heat treatments

Heat Treatment for U10Mo2Zr	Expected Phases from Ternary Phase Diagram	Observed Phases
900˚C Water Quenched	γ-U, Mo$_2$Zr	γ-U, Mo$_2$Zr
650˚C Water Quenched	γ-U, Mo$_2$Zr	γ-U, Mo$_2$Zr

<u>U10Mo + 5 wt.% Zr</u>

In the phase diagram in Figure 39, U10Mo5Zr samples after a 900˚C homogenization, is predicted to be in a two phase region of Mo_2Zr and γ-U. The micrograph from Figure 40 shows that there is Mo_2Zr formation occurring inside the grain and at the grain boundaries of γ-U. The XRD pattern shown in Figure 43 shows that after a 900˚C heat treatment, the U10Mo5Zr sample contains both γ-U and Mo_2Zr peaks. Table 14 shows that the integrated intensity data suggests both the presence of γ-U and Mo_2Zr. The predicted phases from the ternary diagram and observed phases from both XRD and then backscattered SEM micrograph, presented in Table 15, agree well. The lever rule, image analysis and integrated intensities match relatively well. A continued increase in Mo_2Zr wt.% is observed with increased Zr content. Resultantly relative γ-U retention is reduced due to the increased Mo_2Zr formation.

After a 3 hour 650˚C heat treatment, a 3 phase region of Mo_2Zr, γ-U, and α-U is possible according to the 650˚C phase diagram presented in Figure 39. The micrographs in Figure 41 and Figure 42 show the presence of Mo_2Zr and the subsequent destabilization of γ-U. The microstructures present in the micrographs are unclear, however clear increased Mo_2Zr formation is observed. Figure 43 shows the XRD pattern representative of this 650˚C heat treatment for the U10Mo5Zr sample. Figure 43 demonstrates the presence of γ-U, α-U, Mo_2Zr, U_2Mo, and UZr_2. Table 14 shows that UZr_2 is observed in the U10Mo5Zr sample after a 3 hour 650˚C heat treatment utilizing XRD but was not distinguished using image analysis. Table 15 shows that the predicted phases for the 650˚C heat treatment based on the ternary diagrams do not match with the observed phases from XRD and backscattered micrographs. Due to the

composition of the alloy, two γ-U phases of differing content could potentially form, a Zr rich γ-U phase and a Mo rich γ-U phase. After 650˚C and water quenching, it is possible that the local depletion of both Mo and Zr due to the formation of Mo_2Zr, could be causing regions of Zr and Mo rich γ-U to be present. The Mo rich phase could potentially form U_2Mo and the Zr rich phase could form UZr_2. XRD integrated intensities show the potential for both U_2Mo as well as UZr_2. Backscattered mage analysis indicates high α-U presence around the Mo_2Zr grains caused by Mo depletion as is seen by the brighter contrast. The presence of α-U is obvious in the high magnification micrograph, however much more subtle in XRD. UZr_2 was not observed in the micrographs however a peak is clearly visible at around 2θ=46.5˚ in the XRD patterns. Clear γ-U destabilization has occurred. The sharp decrease in γ-U retention is obvious by both image analysis as well as XRD as is presented in Table 15. Higher Mo_2Zr formation is observed as well, causing further Mo depletion in the γ-U phase and in effect causing more γ destabilization in the U10Mo5Zr sample after a 650˚C heat treatment for 3 hours.
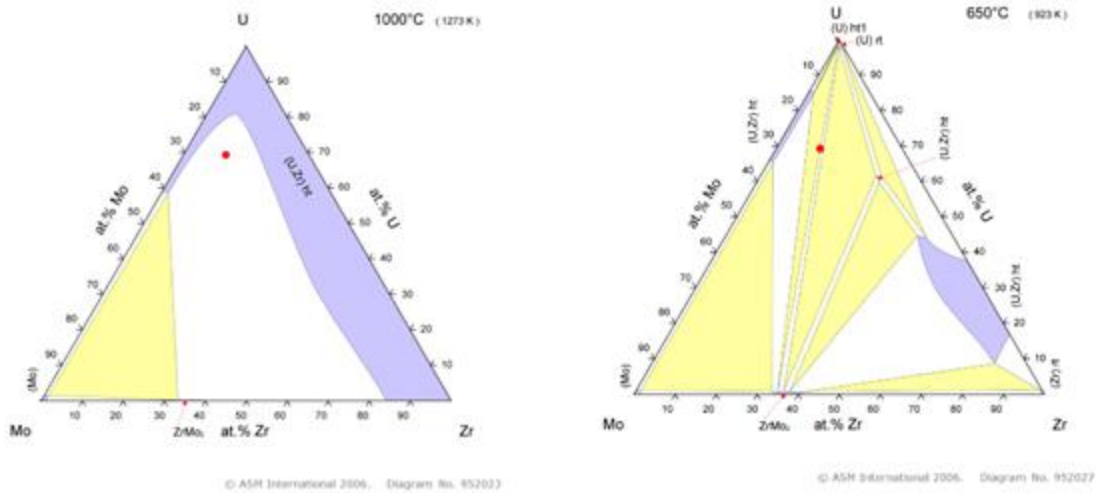
Figure 39 1000˚C and 650˚C U-Mo-Zr phase diagram with U10Mo+5 wt.% Zr composition
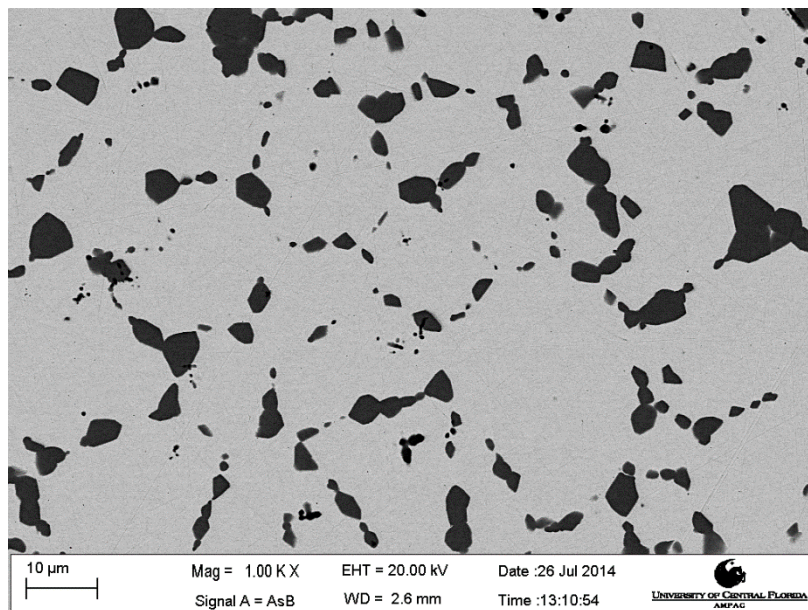
labeled

Figure 40 U10Mo5Zr backscattered micrograph after a 900˚C heat treatment for 168 hours
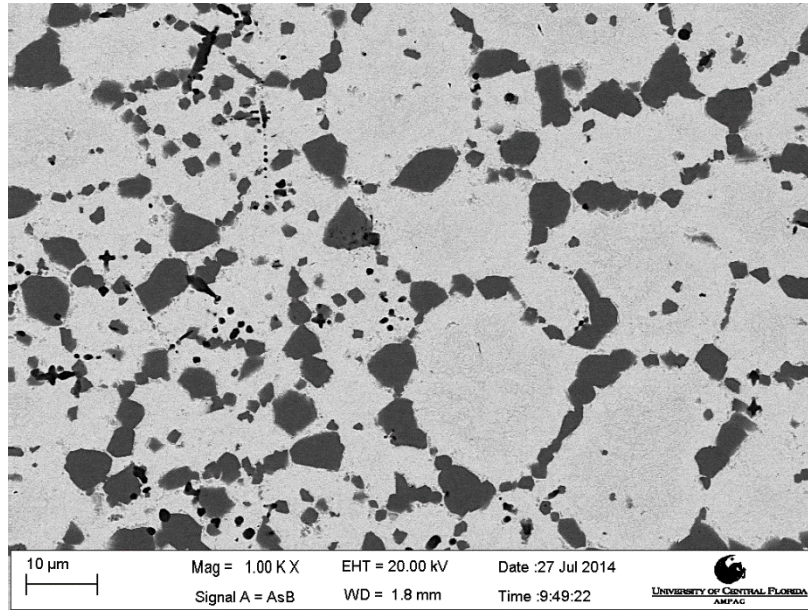
Figure 41 U10Mo5Zr backscattered micrograph after a 650˚C heat treatment for 3 hours

Figure 42 U10Mo5Zr high magnification backscattered micrograph after a 650˚C heat treatment
for 3 hours

Figure 43 XRD pattern for U10Mo5Zr after 900˚C and 650˚C heat treatments

Table 14 Lever rule, image analysis, and integrated intensity results for U10Mo5Zr after 900˚C and 650˚C heat treatments

Sample	Lever Rule	Image Analysis	Integrated Intensity
U10Mo5Zr 900˚C	94.3% γ-U 5.7% Mo_2Zr	93.4% γ-U 6.6% Mo_2Zr	96.2% γ-U 3.8% Mo_2Zr
U10Mo5Zr 650˚C	88.7% α-U 11.3% Mo_2Zr	58.1% γ-U 13.7% Mo_2Zr 18.2% α-U 10.1% U_2Mo	56.8% γ-U 8.0% Mo_2Zr 17.0% α-U 5.6% U_2Mo 14.0% UZr_2

Table 15 Expected and observed phases in the U10Mo5Zr sample after 900˚C and 650˚C heat treatments

Heat Treatment for U10Mo5Zr	Expected Phases from Ternary Phase Diagram	Observed Phases
900˚C Water Quenched	γ-U, Mo_2Zr	γ-U, Mo_2Zr
650˚C Water Quenched	γ-U, Mo_2Zr, α-U	γ-U, Mo_2Zr, α-U, U_2Mo, UZr_2

U10Mo + 10 wt.% Zr

For both 900˚C and 650˚C, the expected phases predicted by the ternary phased diagrams in Figure 44, which contain γ-U and Mo_2Zr after a 900˚C heat treatment and γ-U, Mo_2Zr, and α-U after a 650˚C heat treatment for 3 hours, agree with the observed phases from the backscattered images in Figure 45, Figure 46, and Figure 47. The XRD patterns in Figure 48 indicate that after a 900˚C homogenization step, only γ-U and Mo_2Zr are present. Figure 48 also verifies the presence of γ-U, α-U, and Mo_2Zr after the 650˚C heat treatment. The relative amounts of the phases present are shown in Table 16 and the values presented agree relatively.

The heat treatment of U10Mo10Zr at 900˚C clearly indicates that only γ-U and Mo_2Zr formation occurs and the predicted phases from the ternary phase diagram as well as the observed phases from XRD and backscattered image analysis, presented in Table 17, confirm this observation. The subsequent heat treatment at 650˚C for 3 hours indicates the presence of γ-U, α-U, and Mo_2Zr and is verified by the observations presented in Table 17. The U10Mo10Zr backscattered micrographs after the 650˚C heat treatment contain clear α-U formation along grain boundaries along with some needle-like structures protruding toward the center of the grain of γ-U. As seen by Peterson *et* al. [27] higher Zr content promotes the likelihood of the reaction going to completion and forces this needle-like structure to form shown by the TTT diagram from Repas *et* al. [26]. No UZr_2 is observed in the XRD patterns contrary to the results of Basak *et* al. [22]. Clearly, a higher Zr content is promoting the γ-U destabilization by forming relatively larger amounts of Mo_2Zr and in effect depleting the γ-U of Mo and causing α-U to form at the grain boundaries and in the form of a needle-like structure protruding into the grains.
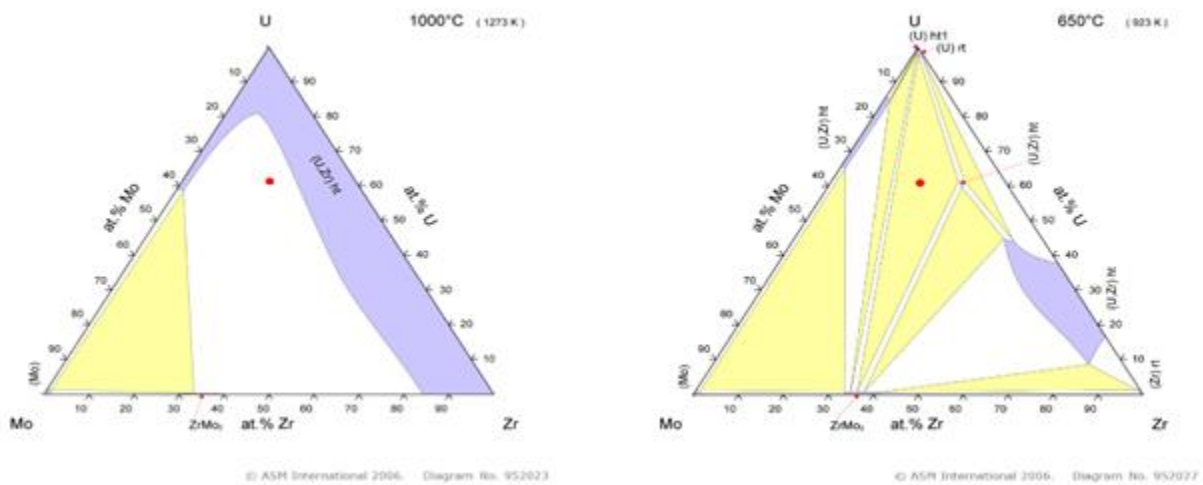
Figure 44 1000˚C and 650˚C U-Mo-Zr phase diagram with U10Mo+10 wt.% Zr composition labeled

Figure 45 U10Mo10Zr backscattered micrograph after a 900˚C heat treatment for 168 hours

Figure 46 U10Mo10Zr backscattered micrograph after a 650˚C heat treatment for 3 hours
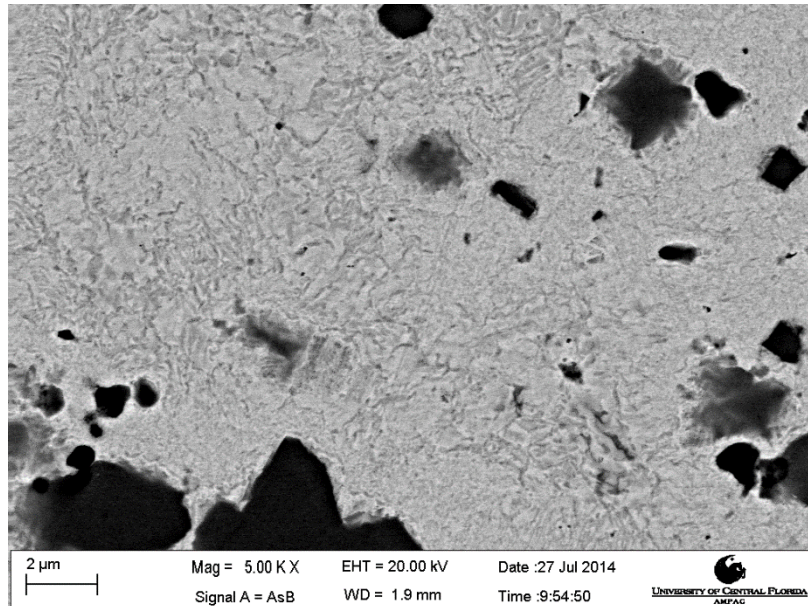
Figure 47 U10Mo10Zr high magnification backscattered micrograph after a 650˚C heat treatment for 3 hours
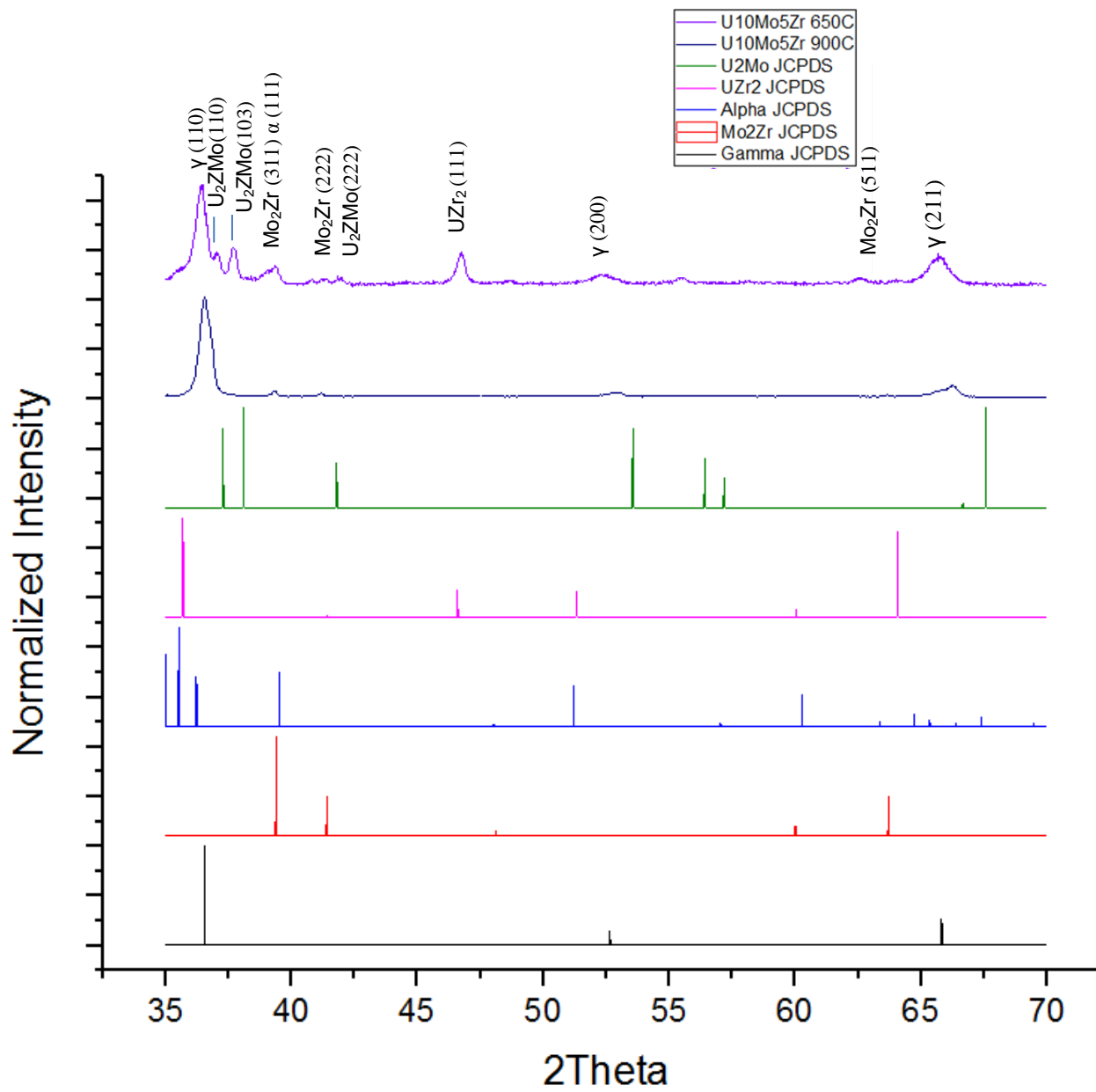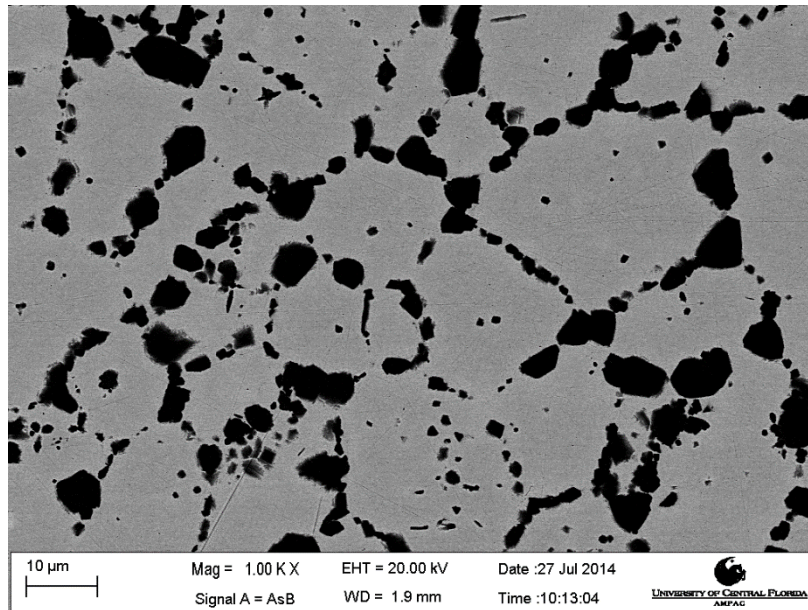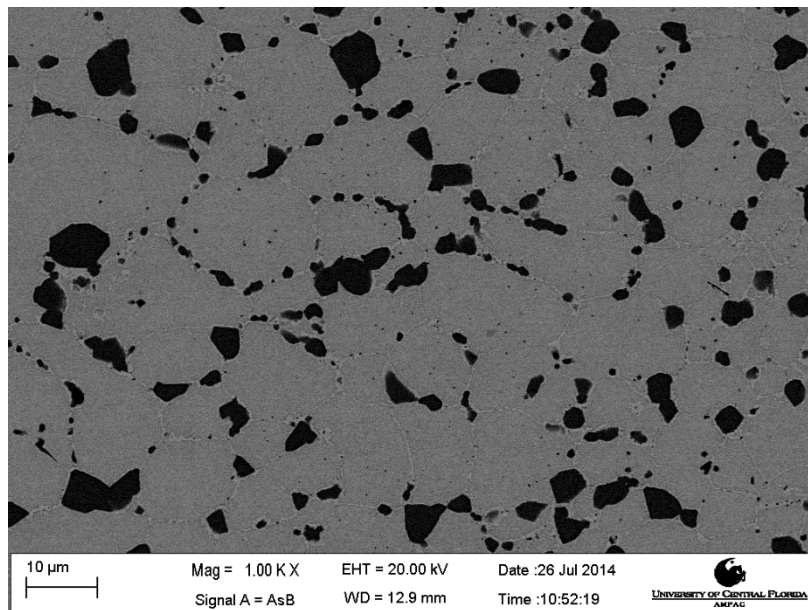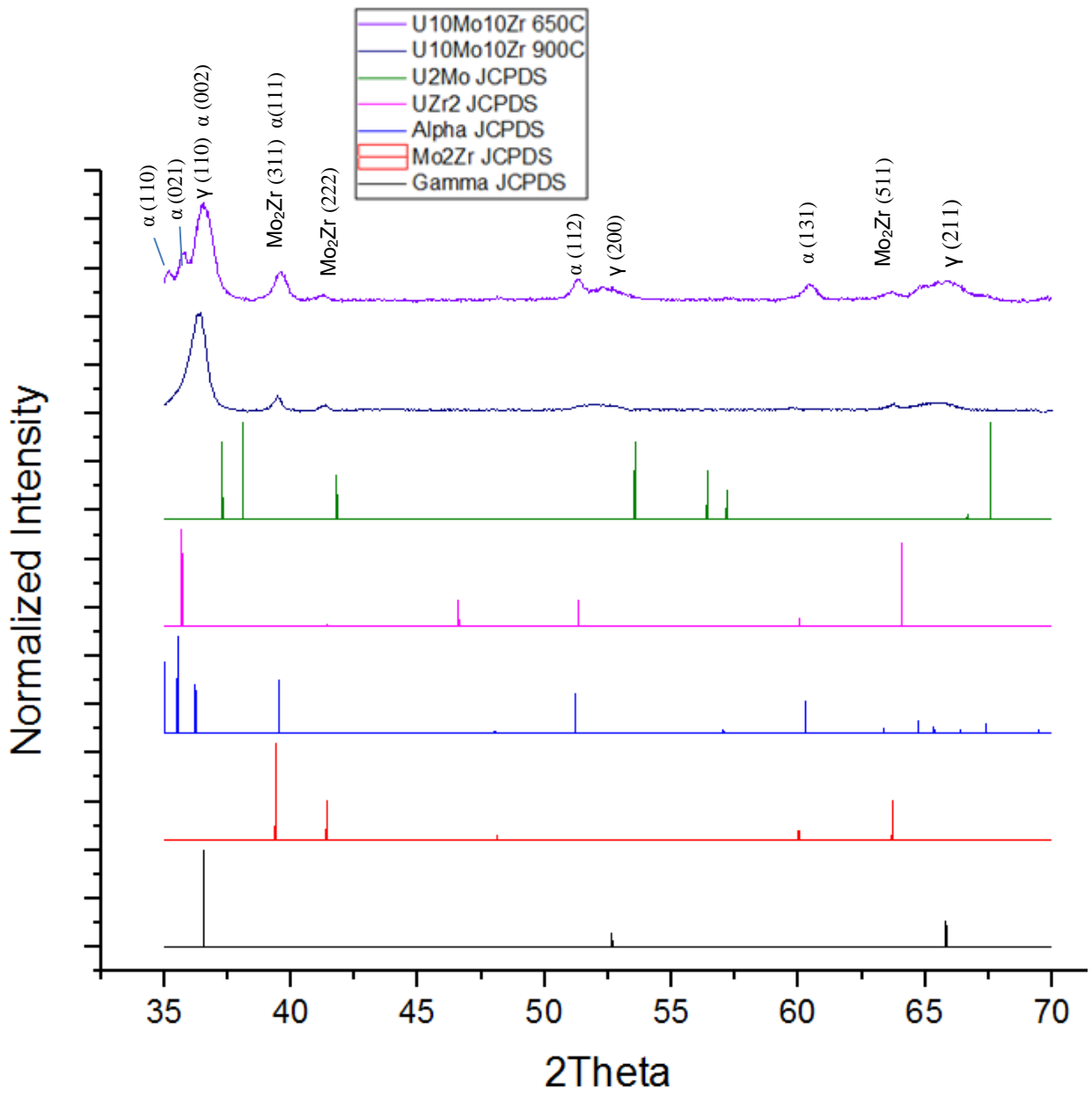
Figure 48 XRD pattern for U10Mo10Zr after 900˚C and 650˚C heat treatments

Table 16 Lever rule, image analysis, and integrated intensity results for U10Mo10Zr after 900˚C and 650˚C heat treatments

Heat Treatments Sample	Lever Rule	Image Analysis	Integrated Intensity
U10Mo10Zr 900˚C	93.4% γ-U 5.6% Mo_2Zr	88.0% γ-U 12% Mo_2Zr	91.1% γ-U 8.9% Mo_2Zr
U10Mo10Zr 650˚C	46.5% γ-U 41.8% α-U 11.7% Mo_2Zr	88.2% γ-U 6.4% Mo_2Zr 5.26% α-U	71.3% γ-U 7.6% Mo_2Zr 25.4% α-U

Table 17 Expected and observed phases in the U10Mo10Zr sample after 900˚C and 650˚C heat treatments

Heat Treatment for U10Mo10Zr	Expected Phases from Ternary Phase Diagram	Observed Phases
900˚C Water Quenched	γ-U, Mo_2Zr	γ-U, Mo_2Zr
650˚C Water Quenched	γ-U, Mo_2Zr, α-U	γ-U, Mo_2Zr, α-U

U10Mo + 20 wt.% Zr

In the U10Mo20Zr sample at both 900 and 650˚C, the ternary diagrams presented in Figure 49 show the potential formation of γ-U and Mo_2Zr after both heat treatments. The backscattered micrographs in Figure 50 and Figure 51 demonstrate the Mo_2Zr formation occurring at the grain boundaries as well as inside the grains of γ-U. XRD patterns presented in Figure 52 show that only two phases, γ-U and Mo_2Zr, form during these heat treatments. The data presented in Table 18 shows that all three methods of quantification agree and the sample only contains two phases. The expected phases from the ternary phase diagrams as well as the observed phases in XRD and backscattered images agree and are presented in Table 19. There is

no alpha being formed as predicted by the ternary phase diagram. Due to the position of the composition of the U10Mo20Zr alloy in the 1000˚C and 650˚C phase diagrams, a small amount of Mo$_2$Zr is predicted to form. By having less Mo$_2$Zr forming, the γ-U phase is more stabilized relative 5 and 10 wt.% Zr samples after both the 900˚C and 650˚C heat treatments.

Figure 49 1000˚C and 650˚C U-Mo-Zr phase diagram with U10Mo+20 wt.% Zr composition labeled
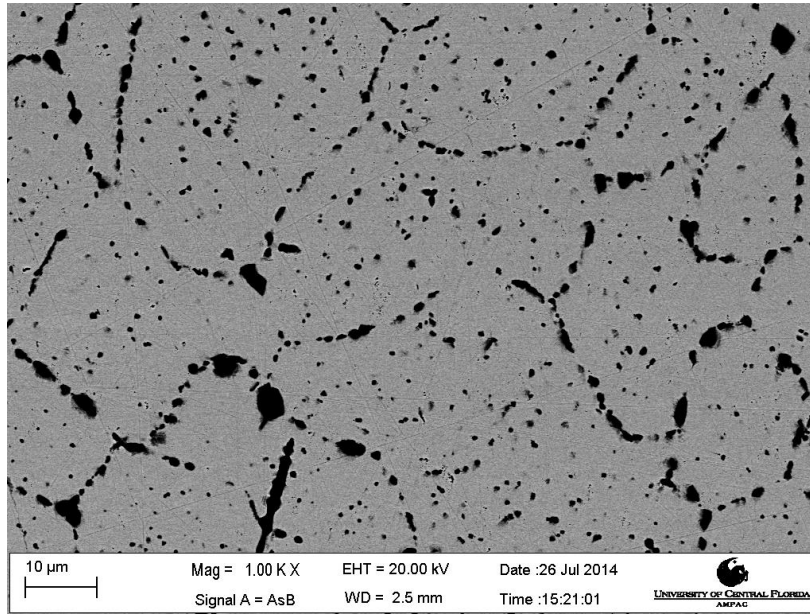
Figure 50 U10Mo20Zr backscattered micrograph after a 900˚C heat treatment for 168 hours

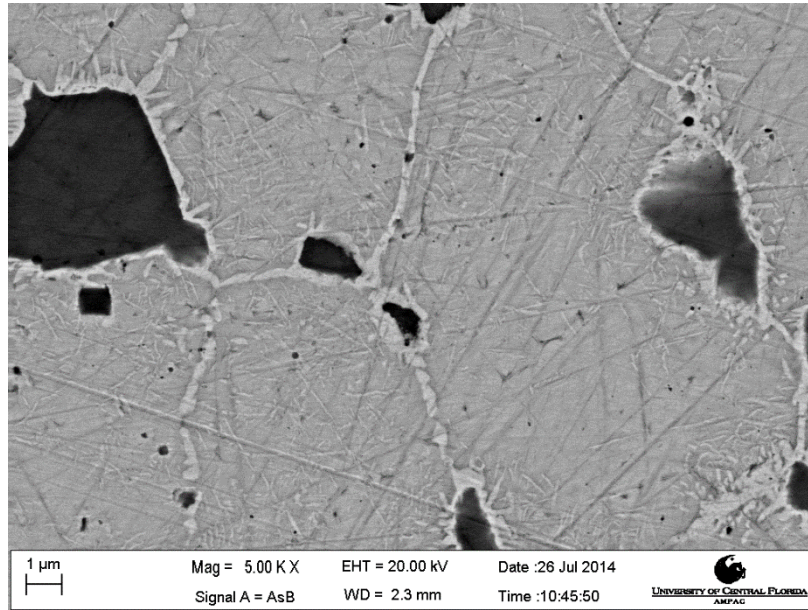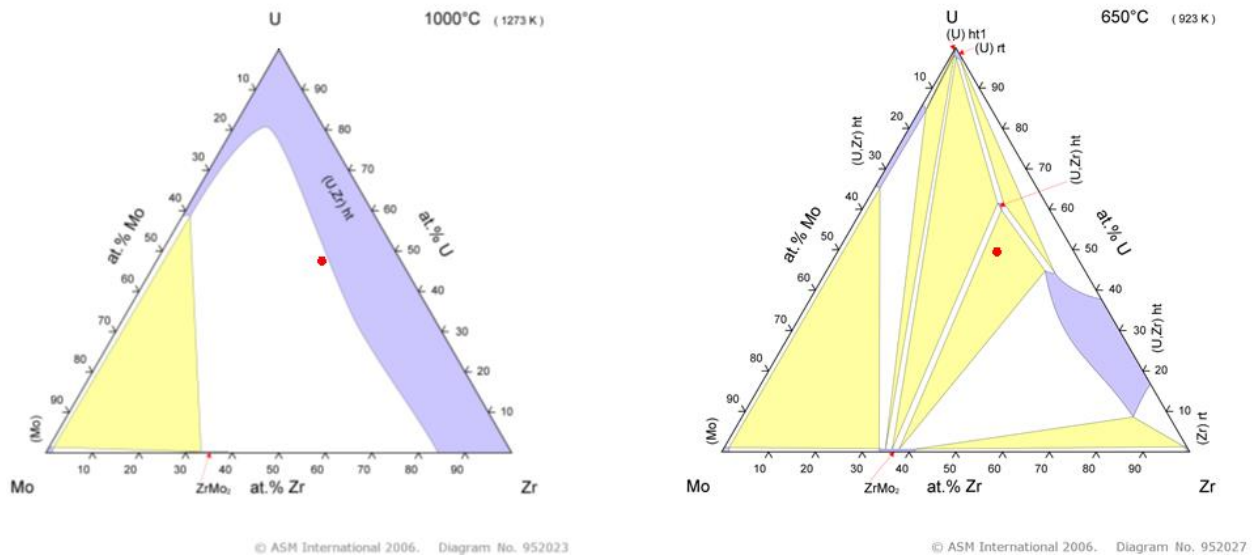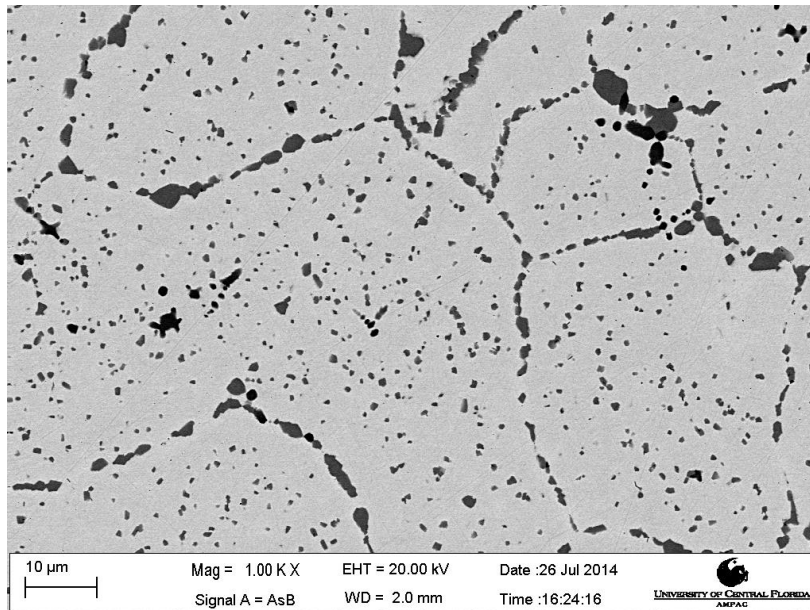Figure 51 U10Mo20Zr backscattered micrograph after a 650˚C heat treatment for 3 hours
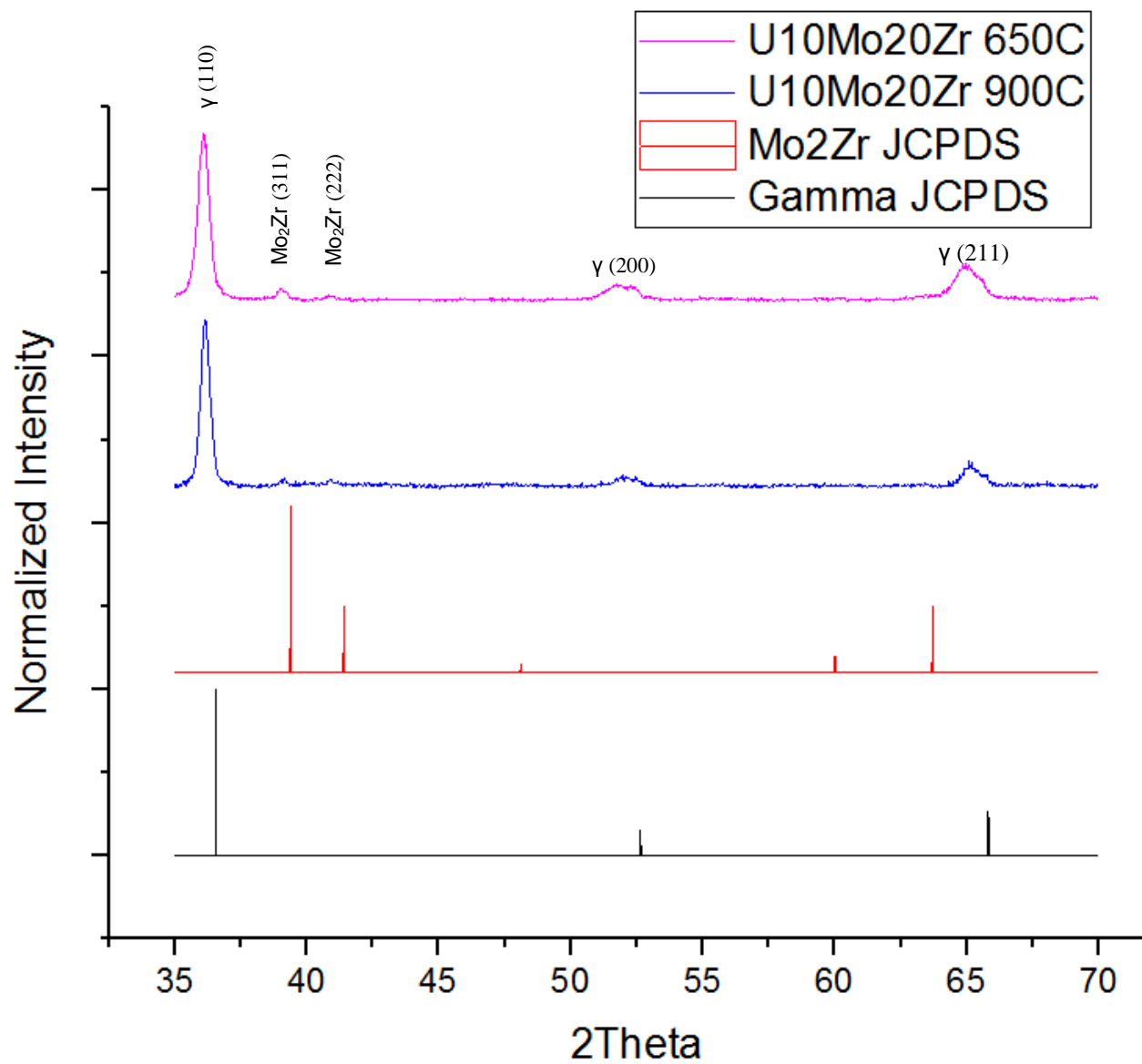
Figure 52 XRD pattern for U10Mo20Zr after 900˚C and 650˚C heat treatments

Table 18 Lever rule, image analysis, and integrated intensity results for U10Mo20Zr after 900˚C and 650˚C heat treatments

Heat Treatments Sample	Lever Rule	Image Analysis	Integrated Intensity
U10Mo20Zr 900˚C	97.4% γ-U 2.6% Mo_2Zr	96.0% γ-U 4.0% Mo_2Zr	95.1% γ-U 4.9% Mo_2Zr
U10Mo20Zr 650˚C	91.5% γ-U 8.5% Mo_2Zr	93.7% γ-U 6.3% Mo_2Zr	97.2% γ-U 2.8% Mo_2Zr

Table 19 Expected and observed phases in the U10Mo20Zr sample after 900˚C and 650˚C heat treatments

Heat Treatment for U10Mo20Zr	Expected Phases from Ternary Phase Diagram	Observed Phases
900˚C Water Quenched	γ-U, Mo_2Zr	γ-U, Mo_2Zr
650˚C Water Quenched	γ-U, Mo_2Zr	γ-U, Mo_2Zr

Trends Observed in the U10Mo + xZr System

To better understand the phases present in the U10Mo + xZr system at each heat treatment step relative to the composition, Figure 53 presents tracked Mo_2Zr content as a function of alloy composition for phases observed after the 900˚C homogenization heat treatment for 168 hours. A clear positive trend is observed with increasing Zr content in the U10Mo + xZr system. Higher Zr content promotes the formation of Mo_2Zr. This graph in Figure 53 shows that integrated intensities from XRD, weight percentages from lever rule analysis, and weight percentages from image analysis all show a similar upwards trend in Mo_2Zr formation with

increasing Zr content. At 10 wt.% Zr, a maximum amount of Mo_2Zr is achieved as is

demonstrated by all three quantifying methods. At 20 wt.% Zr, the composition of the alloy on

the ternary phase diagram indicates a lower Mo_2Zr concentration after a 900˚C heat treatment

and results in a lower Mo_2Zr value for all methods of quantification, however this has yet to be

explained. Due to the empirical nature of the phase diagrams in use, it is very possible that a

revision is in order.

Figure 53 Relative percentages of Mo_2Zr determined by lever rule, integrated intensities, and ImageJ for 900˚C heat treated samples

Figure 54 shows the trend observed in the Mo_2Zr formation for the U10Mo + xZr alloys

after the 650˚C heat treatment for 3 hours. Once again, increased Zr content promotes the

formation of Mo_2Zr. A clear upwards trend is observed for all methods used for quantification.

At 10 wt.% Zr, α-U formation forces the Mo_2Zr content to be lower than was observed for the

900˚C heat treated samples regarding integrated intensities and backscattered micrographs. The 5

wt.% Zr alloy contains the highest Mo_2Zr formation according to image analysis and the

integrated intensities. Once again the composition of the U10Mo20Zr sample caused a relative

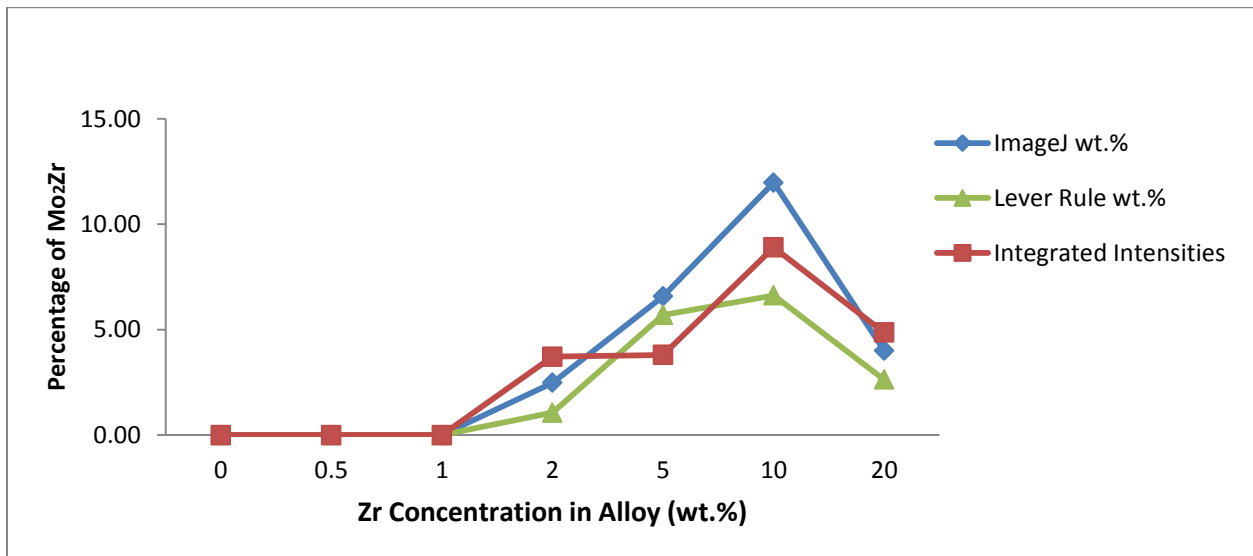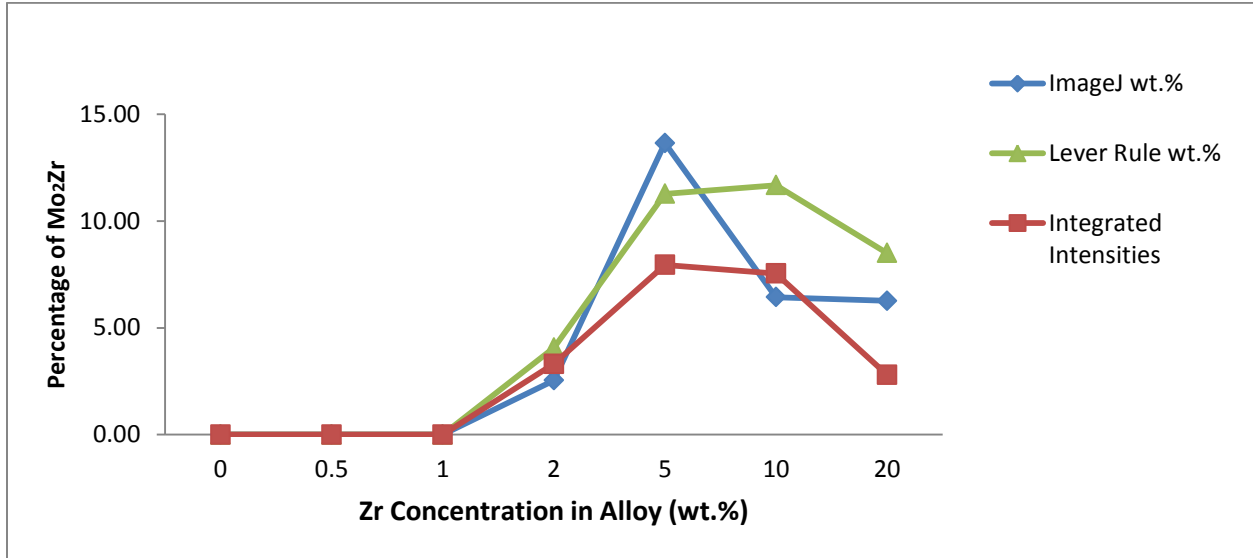decrease in the amount of Mo_2Zr formed after the 650˚C heat treatment.

Figure 54 Relative percentages of Mo_2Zr determined by lever rule, integrated intensities, and ImageJ for 650˚C heat treated samples

CHAPTER 5: SUMMARY AND CONCLUSION

A general increase in Mo_2Zr formation was observed with increasing Zr content in the U10Mo+Zr samples after a 900˚C homogenization and a 650˚C 3 hour heat treatment. Increased Zr content destabilized the γ-U phase by forming Mo_2Zr with the γ-U stabilizing Mo.

At 900˚C no α-U formation occurred, however the Mo_2Zr content that was a result of the addition of Zr effectively reduced the γ-U content of the U10Mo + xZr samples (x=0.0, 0.5, 1.0, 2.0, 5.0, 10.0, and 20.0 wt.% Zr). In the alloys with Zr concentrations from 0 to 1 wt.% Zr, no Mo_2Zr was observed in either the backscattered micrographs or the XRD patterns after the 900˚C heat treatment. The ternary diagram predicted that only a γ-U phase would exist at these compositions and temperatures. In the 0.5 and 1.0 wt.% Zr samples after a 900˚C homogenization, Zr rich precipitates were observed via backscatter SEM. In the alloys containing 2 to 20 wt.% Zr, Mo_2Zr formation occurred after the 900˚C homogenization heat treatment. Sufficient Zr content enabled the formation of Mo_2Zr in and around the grains of γ-U. Image analysis and integrated intensities agreed with the predicted amounts of Mo_2Zr formation from the ternary diagram for these samples. As the Zr content increased, so too did the presence of Mo_2Zr after the heat treatment. In the 20 wt.% Zr alloy, a relatively smaller amount of Mo_2Zr was formed after the 900˚C heat treatment.

After a 3 hour 650˚C heat treatment representative of the hot rolling step in the HIP process, increased Mo_2Zr formation was observed for all alloys above 1 wt.% Zr. The alloys containing 0.0, 0.5, and 1.0 wt.% Zr did not form Mo_2Zr, however in the 0.5 and 1.0 wt.% Zr samples a Zr rich precipitate was observed. The ternary phase diagrams predicted that after a

650°C heat treatment, no Mo_2Zr would be formed for these low Zr concentration alloys. The alloys which contained more than 2 wt.% Zr exhibited higher Mo_2Zr formation and in some cases, relatively higher γ-U destabilization. In the 5 wt.% Zr alloy, the backscattered micrographs demonstrated Mo_2Zr formation along with a microstructure which was unclear. XRD analysis and ternary diagram analysis indicated that for this sample, there was the potential of UZr_2 and U_2Mo formation due to two different compositions of γ-U, a Zr rich and a Mo rich composition. The alloy containing 10 wt.% Zr showed clear α-U formation along the grain boundaries as well as in needle-like protrusions toward the center of the grain. At 20 wt.% Zr the alloy did no show enough Mo_2Zr formation and in effect, no significant γ-U destabilization occurred. After a 650°C heat treatment, an upward trend in Mo_2Zr formation was observed. Higher Zr concentrations promoted the formation of Mo_2Zr. The Mo depletion that occurred due to this Mo_2Zr formation, caused a γ-U to α-U transformation.

The anisotropic swelling behavior of this α-U phase which occurs under irradiation is an undesirable quality. In monolithic fuel plates containing an U10Mo fuel meat with a Zr barrier, interdiffusion and reaction during the fabrication process of HIP plates will occur and form Mo_2Zr. The resultant Mo depletion from the fuel meat will produce the α-U phase. High temperature processing to try to avoid the formation of α-U will still cause γ-U destabilization due to the potential formation of the Mo_2Zr phase at high temperatures. Subsequent heat treatments would then allow for α-U formation to occur later in the processing. Considering this, a Zr barrier is not advised unless the processing of the monolithic fuel plates is monitored extremely carefully.

REFERENCES

1.   Wachs, D., *RERTR Fuel Developmemt and Qualification Plan*. 2007, Idaho National Laboratory (INL).

2.   Meyer, M., et al. *Irradiation Behavior of Uranium-Molybdenum Dispersion Fuel: Fuel Performance Data from RERTR-1 and RERTR-2*. in *Proc. Inter. Meeting on RERTR-1999*. 1999.

3.   Meyer, M., et al., *Low-temperature irradiation behavior of uranium–molybdenum alloy dispersion fuel.* Journal of Nuclear Materials, 2002. **304**(2): p. 221-236.

4.   Meyer, M., et al. *Metallographic analysis of irradiated RERTR-3 fuel test specimens*. in *Proc. of the 2000 International Meeting on Reduced Enrichment for Research and Test Reactors, ANL/TD/TM-01-12, Las Vegas, Nevada*. 2000.

5.   Neogy, S., et al., *Microstructural study of gamma phase stability in U–9wt.% Mo alloy.* Journal of Nuclear Materials, 2012. **422**(1): p. 77-85.

6.   Leenaers, A., et al., *Post-irradiation examination of uranium–7wt% molybdenum atomized dispersion fuel.* Journal of Nuclear Materials, 2004. **335**(1): p. 39-47.

7.   Wachs, D., et al., *High density fuel development for research reactors*. 2007, Idaho National Laboratory (INL).

8.   Huang, K., et al., *Diffusion Barrier Selection from Refractory Metals (Zr, Mo and Nb) Via Interdiffusion Investigation for U-Mo RERTR Fuel Alloy.* Journal of phase equilibria and diffusion, 2014. **35**(2): p. 146-156.

9.   Brandes, E. and G. Brook, *Smithells metals reference book, 1992.* London, But.

10.   Sears, V.F., *Neutron scattering lengths and cross sections.* Neutron news, 1992. **3**(3): p. 26-37.

11.   Metals, A.S.f. and J.R. Davis, *ASM handbook. 2. Properties and selection: nonferrous alloys and special-purpose materials*. 2009: ASM international.

12.   Moore, G.A., et al. *Monolithic fuel fabrication process development at the Idaho National Laboratory*. in *RERTR 2009-31st International Meeting on Reduced Enrichment for Research and Test Reactors*. 2009.

13.   Huang, K., et al., *Interdiffusion between Zr diffusion barrier and U-Mo alloy.* Journal of Phase Equilibria and Diffusion, 2012. **33**(6): p. 443-449.

14.   Park, Y., et al., *Growth kinetics and microstructural evolution during hot isostatic pressing of U-10wt.% Mo monolithic fuel plate in AA6061 cladding with Zr diffusion barrier.* Journal of Nuclear Materials, 2014. **447**(1): p. 215-224.

15.   Perez, E., et al., *Microstructural analysis of as-processed U–10wt.% Mo monolithic fuel plate in AA6061 matrix with Zr diffusion barrier.* Journal of Nuclear Materials, 2010. **402**(1): p. 8-14.

16.   Eisenhower, D.D., *Atoms for peace.* IAEA BULLETIN, 2003. **45**(2): p. 62-67.

17.   Wiencek, T., *Summary report on fuel development and miniplate fabrication for the RERTR program, 1978 to 1990.* 1995, Argonne National Lab., IL (United States).

18.   Feraday, M., et al., *Irradiation behaviour of a corrosion resistant U-Si-Al fuel alloy.* 1975, Atomic Energy of Canada Ltd., Chalk River, Ontario. Chalk River Nuclear Labs.

19.   Hofman, G., R. Domagala, and G. Copeland, *Irradiation behavior of low-enriched U 6 Fe-Ai dispersion fuel elements.* Journal of Nuclear Materials, 1987. **150**(2): p. 238-243.

20.   Meyer, M., et al., *Irradiation behavior of U 6 Mn–Al dispersion fuel elements.* Journal of nuclear materials, 2000. **278**(2): p. 358-363.

21.   T.R.G Kutty, S.D., Joydipta Banerjee, Santu Kaity, Arun Kumar, C.B. Basak, *Thermophysical properties of U2Mo Intermetallic.* Journal of Nuclear Materials, 2012. **402**(1-3): p. 193-197.

22.   Chandrabhanu Basak, R.K., G.J. Prasad, H.S. Kamath, N. Prabhu, S. Banerjee, *Investigation on the martensitic transformation and the associated intermediate phase in U-2 wt%Zr alloy.* journal of Nuclear Materials, 2009. **393**(1): p. 146-152.

23.   A. Paz y Puente, J.D., D.D. Keiser Jr, Y.H. Sohn, *Investigation of interdiffusion behavior in the Mo-Zr binary system vis diffusion couple studies.* Int. Journal of Refractory Metals and Hard Materials, 2013. **43**: p. 317-321.

24.   Rosa Jerlerud Perez, B.S., *Thermodynamic assessment of the Mo-Zr binary phase diagram.* Computer Coupling of Phase Diagrams and Thermochemisty, 2003. **27**: p. 253-262.

25.   O.S. Ivanov, G.N.B., *Isothermal Cross Sections of the Triple System Uranium-Molybdenum-Zirconium at 1000˚C-625˚C.* Struct. Alloys Certain Systems Cont. Uranium Thorium, 1963.

26.   P.E. Repas, R.H.G., R.F. Hehemann, *Transformation Characteristics of three Uranium base Alloys.* 1963.

27. C. A. W. Peterson, W.J.S., S. L. DiGiallonardo, *Isothermal Transformation Study of Some Uranium-Base Alloys.* 1964.

28. C. Suryanarayana, M.G.N., *X-Ray Diffraction, A Practical Approach.* 1998: p. 223-230.

29. Goldstein, J., *Scanning Electron Microscopy and X-Ray Microanalysis: A text for Biologists, materials Scientists, and Geologists.* Science, 2012.

30. CIAAW, *Atomic weights of the elements 2015.*

31. Lab, J., *The Element Molybdenum.*

32. Lab, T.J., *The Element Zirconium.*